1 # Catchment-scale heterogeneity of flow and storage properties in a weathered/fractured hard rock aquifer from resistivity and magnetic resonance surveys: Implications for groundwater flow paths and residence times distributions

6 J-C. Comte[1,*], U. Ofterdinger[2], A. Legchenko[3], J. Caulfield[4], R. Cassidy[5], J. A. Mézquita González[1]

8 [1]University of Aberdeen, School of Geosciences, Aberdeen AB24 3UF, UK
9 [2]Queen's University Belfast, School of Natural and Built Environment, Belfast BT9 5AG, UK
10 [3]IRD/Université Joseph Fourier, Grenoble, France
11 [4]Trinity College Dublin, School of Natural Sciences, Department of Geology, Dublin 2, Ireland
12 [5]Agri-Food and Biosciences Institute (AFBI), Belfast BT9 5PX, UK
13 *Correspondence (jc.comte@abdn.ac.uk)

15 **Running Title**
16 Flow and storage properties of fractured rocks

18 **Abstract**

19 *Groundwater pathways and residence times are controlled by aquifer flow and storage properties,*
20 *which are characterised by high spatial heterogeneity in weathered/fractured hard rock aquifers.*
21 *Building on earlier work in a metamorphic aquifer in NW Ireland, new clay mineralogy and*
22 *geophysical data analyses provided high spatial resolution constraints on the variations of aquifer*
23 *properties. Groundwater storage values derived from magnetic resonance sounding and electrical*
24 *resistivity tomography were found to largely vary laterally and with depth, by orders of magnitude.*
25 *Subsequent implementation of numerical, 2D-hillslope groundwater models showed that*
26 *incorporating heterogeneity from geophysical data in model parametrisation led to best fit to*
27 *observations as compared to a reference model based on borehole data only. Model simulations*
28 *further revealed that; 1/strong spatial heterogeneity produces deeper, longer groundwater flow*
29 *paths and higher age mixing in agreement with the mixed sub-modern/modern ages (mostly <50*
30 *years) provided by independent tritium data; 2/areas with extensive weathering/fracturing are*
31 *correlated with seepage zones of older groundwater, due to changes in the flow directions, and are*
32 *likely to act as drainage structures for younger groundwater on a catchment or regional scale.*
33 *Implications for groundwater resilience to climate extremes and surface pollution are discussed along*
34 *with recommendations for further research.*

35 Weathered/fractured hard rock aquifers underlie over 20% of the global land surface (Sharp
36 2014) and are characterised by a high degree of structural heterogeneity and overall low
37 productivity. In recent years, water managers and policy-makers have moved to adopt a catchment
38 scale approach to the integrated management of surface and subsurface water resources (EU Water
39 Framework Directive 2000/60/EC), including the UK (UKTAG 2011) and Ireland (Daly *et al*. 2016).
40 Understanding spatial variations of aquifer hydraulic properties at the catchment-scale, which
41 dictates groundwater flow pathways and residence times, is crucial to inform catchment
42 management plans. Yet, resolving such spatial heterogeneity in fractured bedrock remains very
43 challenging due to the typically scattered nature of direct observations points (boreholes and
44 outcrops) that usually do not have sufficient spatial coverage to capture the scale of heterogeneity
45 (De Marsily *et al*. 2005; Neuman 2005).
46 To address the lack of spatial resolution in heterogeneous fractured rock catchments, traditional
47 direct testing techniques in boreholes, such as hydraulic testing and geophysical logging, are
48 increasingly combined with indirect and more spatially integrative investigation methods, including
49 tracer testing (e.g. Klepikova 2016), geophysical imaging (ground- or airborne-based) (Comte *et al*.
50 2012; Shakas *et al*. 2016; Day-Lewis *et al*. 2017) and remote sensing (Cassidy *et al*. 2014; Frances *et*
51 *al*. 2014). The use of geophysics has long proven effective in resolving, at catchment scale, the
52 heterogeneity of fractured rock aquifers (Holbrook *et al*. 2014; Robinson *et al*. 2016). The Electrical
53 Resistivity Tomography (ERT) method is known to be efficient at imaging spatial variability in
54 weathering, geological heterogeneity and fracture patterns (e.g. Chandra *et al.* 2010; Rainer *et al*.
55 2007). All ERT studies, however, stress the importance of *a priori* information, especially borehole
56 data and outcrop mapping to support its hydrogeological interpretation (Skinner & Heinson 2004;
57 Comte *et al.* 2012).
58 A number of studies have demonstrated the benefits of using ERT in combination with other
59 geophysical methods; in particularly with the magnetic resonance sounding (MRS) that complements
60 imaging of heterogeneity by ERT with lower resolution but more quantitative information on water
61 storage. Both methods have, for instance, been used to map groundwater occurrence and develop
62 hydrogeological conceptual and numerical models in weathered basement aquifers (Frances *et al.*
63 2014; Baltassat *et al.* 2005) and monitor groundwater recharge (Descloitres *et al.* 2008). As yet,
64 however, most of these studies have focused on low latitude regions with deep and relatively water-
65 productive weathering horizons (saprolite) that produce strong MRS and ERT responses for relatively
66 simple, layered aquifer geometries. There are fewer examples in higher latitude catchments with a
67 glacial legacy, such as in Ireland, where most of the saprolite (relatively high storage, porous layer) is
68 absent, exposing only the fractured (low storage) and structurally complex bedrock. In addition,
69 these geophysical approaches still remain either (i) not systematically applied in catchment
70 groundwater studies or (ii) applied qualitatively, i.e. used to inform aquifer heterogeneity conceptual
71 models rather than to quantify spatial variations in aquifer properties (permeability and porosity).
72 This needs further consideration in highly heterogeneous basement rock catchments.
73 In Ireland, the fractured rock aquifers provide a good analogue of temperate region bedrock
74 aquifers with a glacial legacy. The island of Ireland is underlain by over 60**%** of hydrogeologically
75 poorly-productive fractured bedrock (Moe *et al.* 2010), either cropping out directly or covered by
76 superficial glacio-fluvial and/or alluvial sediments. Most of this poorly-productive bedrock is
77 composed of various grades of metamorphic (basement) rocks; from low-grade metasediments to
78 high-grade gneiss-migmatites and granitoids. Groundwater in these rocks, despite their overall low
79 productivity, is nonetheless crucial for maintaining river base flow during dry periods and supporting
80 aquatic ecosystems and small-scale rural water supply (DCCAE 2017). Over the last decade, the
81 extension of the Irish national groundwater monitoring network to poorly productive basement
82 aquifers as part of implementing the European Union's Water Framework Directive (EPA 2006; Moe
83 *et al.* 2010) has stimulated hydrogeological research through Irish Government-funded projects.
84 Among them, the Griffith Poorly-productive Aquifers Project (2007-2014), on which this work is
85 based, aimed to improve the understanding of groundwater flow regimes in fractured rock aquifers

86 and the contribution of groundwater to catchment water balance (Comte *et al.* 2012; Cassidy *et al.*
87 2014; Caulfield *et al.* 2014; Cai & Ofterdinger 2016).
88   This paper presents an overview of the latest research in a micaschist catchment in Co. Donegal,
89 Republic of Ireland, with the aim of resolving catchment-scale spatial variations of aquifer
90 properties. It synthesises previously published research on aquifer typology and well-scale hydraulics
91 (Comte *et al.* 2012; Cassidy *et al.* 2014), bedrock weathering (Caulfield *et al.* 2014) and aquifer
92 storage properties (Legchenko *et al.* 2017), augmented with the latest results from quantitative
93 interpretation of geophysical data (ERT and MRS) to provide a robust spatial understanding of flow
94 and storage property fields. This work further explores the integration of the existing knowledge on
95 the heterogeneity of aquifer properties using numerical models to assess groundwater flow paths
96 and residence time distributions. Finally, we use the results to discuss the impact of climate change
97 and contaminant transport on groundwater resources and catchment management, as well as
98 further recommendations for improved groundwater modelling.
99
100
101 **Hydrogeological setting**
102
103 *Geology*
104
105   The Gortinlieve catchment (5 km^2), Co. Donegal, NW Ireland (Figure 1) is underlain by Late
106 Precambrian micaschists and psammites of intermediate metamorphic grade (low amphibolite
107 facies). These belong to the Grampian terrane in Co. Donegal as part of the Southern Highland
108 Group, spanning through Ireland and Scotland. They originate from turbidite sequences deposited c.
109 550 Ma BP (McConnell & Long 1997; Caulfield *et al.* 2014) and subsequently subjected to poly-phase
110 deformation and metamorphism during the Caledonian orogeny. The Caledonian tectonic regime
111 associated with the closure of the Iapetus Ocean (Grampian phase, early Ordovician) generated the
112 current regional NE–SW oriented structures (Chew 2009) characterised by fault scarps and
113 cartographic/topographic lineaments visible in the upper catchment (Fig. 1). The later Taconic phase
114 (late Ordovician) generated the current WNW-ESE orientation deformational structures and
115 imprinted the retrograde amphibolite metamorphic facies (McConnell & Long 1997). The current,
116 Alpine, strike-slip tectonic regime, is reflected by reactivation of NE-SW fracture orientations and
117 further creation of a general NW-SE trend (Worthington & Walsh 2011; Cooper *et al.* 2012).
118 Localised kaolinite rich Tertiary lateritic horizons preserved on Grampian rocks of western Ireland
119 (Legg *et al.* 1985) provide evidence that the basement was during this time at least partially
120 exhumed and undergoing tropical weathering. Subsequent Quaternary glaciations have resulted in
121 further erosion, including the removal of the upper levels of the weathering profiles, most
122 pronounced in high topographic areas, and in the deposition of heterogeneous glacio-fluvial material
123 (clay-till and sand and gravel) in low-lying areas and valley bottoms.
124
125 *Hydrogeology and borehole instrumentation*
126
127   Annual rainfall in the area ranges from 1000 to 1200 mm and mean temperature annually ranges
128 from 6 to 14 °C (Met Eireann 2017). The catchment comprises a headwater stream network of a
129 Carrigans River, a tributary of the River Foyle that discharges into the Atlantic Ocean, approx. 40 km
130 NE of the catchment (Caulfield *et al.* 2014). The Gortinlieve catchment was instrumented with
131 monitoring boreholes by the Irish Environmental Protection Agency (EPA) in 2006 as part of the
132 national groundwater monitoring programme. Three borehole clusters were sited in a linear
133 hillslope transect at high (GO1, 174 m above mean sea level; hereafter noted m amsl), intermediate
134 (GO2, 88 m amsl) and low (GO3, 33 m amsl) elevations within the catchment. Individual clusters
135 contain up to 4 boreholes, each isolated and screened across different depth-distinctive zones
136 commonly encountered in Irish bedrock aquifers. The initial classification of Moe *et al.* (2010)

137 conceptually described these respective intervals as; subsoil SS (average interval 1–3 m below
138 ground surface (bgs); only present in Gortinlieve at the valley bottom), transition zone T (average
139 interval 4–5 m bgs), shallow bedrock S (average interval 8–19 m bgs) and deep bedrock D (average
140 interval 30–67 m bgs). The conceptual model was further refined by Comte *et al.* (2012) in order to
141 help reconcile geological features with geophysical constraints (Fig. 2): overburden deposits (cf.
142 subsoil); broken bedrock (cf. transition zone); fissured bedrock (cf. shallow bedrock); massive
143 bedrock (cf. deep bedrock). The Irish EPA monitors water levels at 15-minute intervals in each
144 borehole using automatic data loggers. The site was also equipped with an automated tipping
145 bucket rain gauge (AEG 100) since October 2010 for the duration of the project.
146
147
148 **Aquifer characterisation methods**
149
150 *Structural, mineralogical and hydraulic investigations*
151
152   Detailed analysis of fracture patterns and clay occurrence in the bedrock was carried out in order
153 to establish the micro- to meso-scale structural controls on groundwater flow, and to provide
154 constraints on larger (meso- to macro) scale hydraulic and geophysical interpretations and numerical
155 modelling.
156   Fracture orientations were measured on maps, outcrops, boreholes and quarry exposures.
157 Regional structural trends were determined from interpretation of the geological map (Smith 1991;
158 Long et al. 1992; McConnell & Long 1997) and the 20-m resolution digital elevation model (Ordnance
159 Survey of Ireland). During field mapping, the main fracture parameters measured were strike, dip
160 magnitude, dip azimuth with a minimum of 30 fracture measurements for each sample site,
161 subsequently plotted as rose diagram and Schmidt net pole density distribution. The acquisition and
162 plotting methodology are described in details in Comte *et al.* (2012) and Nitsche (2014). Borehole
163 fractures were analysed using acoustic televiewer logs. Among these, hydraulically active fractures
164 were identified through cross-correlation with electrical conductivity logs whereby marked changes
165 in water electrical conductivity at the depth of observed fractures was interpreted as fracture flow
166 (Nitsche 2014).
167   Mineralogical and petrographic data are summarised by Caulfield *et al.* (2014). Representative
168 field outcrop and recovered borehole core samples were further characterised in this study to
169 quantify the relative proportions of identified phyllosilicate minerals to assess their influence on
170 geoelectrical properties. The mineral modes of the dominant basement lithologies (psammitic
171 schists uphill vs. micaschists downhill) were quantified by petrographic point-counting (500 points
172 per slide). These compositions were taken to represent fresh, primary (unweathered) bedrock. Free
173 phyllosilicate minerals (mineral grains not bound in the competent fresh bedrock structure) were
174 separated and collected from weathered samples by repeated washing with distilled water and dried
175 at 50°C. Clay sized (<2 μm) fractions were obtained following the method outlined in Caulfield *et al*.
176 (2014), and references therein. The relative proportions of primary (muscovite, chlorite) and
177 secondary (illite, montmorillonite and illite/montmorillonite admixtures) were determined via
178 thermogravimetric analysis (TGA) using a Netzsch libra thermogravimetric analyser, in conjunction
179 with XRD and FTIR results from Caulfield *et al*. (2014). Samples were heated from 200-880°C to
180 determine sequential dehydroxylation water loss from the clay mineral fraction. Mineral proportions
181 (volume %) were converted to weight %. Using the method of Revil *et al*. (1998), the total cation
182 exchange capacity (CEC) of the different geological units (transition, shallow, deep bedrock) at each
183 of the three sites (GO1-3) were calculated from (i) the relative mass proportion of clay minerals, (ii)
184 their individual CEC, obtained from literature (Swineford 1955; Carroll 1959; Wiklander 1964;
185 Thomas 1976; Ridge 1983; Revil *et al*. 1998; Crain 2000; Gillespie *et al*. 2001; Ellis & Singer 2007;
186 Henn *et al*. 2007) and (iii) the total clay content derived from natural gamma ray logs from each
187 borehole.

188   Aquifer pumping and recovery tests were implemented in every borehole to provide local values
189   of equivalent hydraulic conductivity and storativity for each borehole. The hydraulic testing
190   methodology is described in details in Comte *et al*. (2012). Pumping test were conducted at a
191   constant rate (2 to 30 L/min depending on the borehole) and both pumping and recovery curves
192   were jointly interpreted using AQTESOLV Pro v4.5 and applying a range of adapted analytical
193   solutions (with regards to the known aquifer structure and the borehole technical characteristics)
194   including single porosity/permeability models. Hydraulic conductivities (K) were calculated from
195   transmissivity values using observed unit aquifer thicknesses from borehole data, ERT data and
196   geophysical logging data.
197   K in fractured rocks is typically anisotropic, i.e. directionally dependent implying different K
198   values in different directions, with the maximum hydraulic conductivity $Kmax$ following the direction
199   of the hydraulic active fractures and the minimum hydraulic conductivity $Kmin$ being orthogonal to
200   the hydraulic active fractures. This further implies that the anisotropy angle in fractured rocks,
201   because of the presence of steep fractures, has a higher vertical component than in most
202   sedimentary rocks where the direction of $Kmax$ is often sub-horizontal, parallel to the sedimentary
203   bedding (in this case $Kmax$ is usually denoted Kh) and the direction $Kmin$ is subvertical (and in this
204   case denoted Kv). In this work, values of hydraulic conductivities provided by hydraulic tests were
205   further analysed in terms of anisotropy in 2D (along the studied transect). As hydraulic test values
206   were assumed equivalent to isotropic hydraulic conductivities, the integration of fracture analysis
207   data allowed for the definition of $Kmax$ $Kmin$ and anisotropy angles (by definition the angle of $Kmax$
208   to the horizontal) based on the measured orientation of the hydraulically active fractures. The
209   anisotropy ratio $Kmin/Kmax$ (unitless) was derived by considering it to decrease with depth from 0.5
210   to 0.1. At depth, where the steep fracture sets dominated (see section *Aquifer characterisation*
211   *results*) and produced a stronger anisotropy, the ratio was set to 0.1, whereas at shallow depths,
212   where other fracture sets and pronounced weathering contribute to flow, particularly in the broken
213   bedrock, anisotropy was expected to weaken and was therefore set to 0.5. The anisotropy angle was
214   derived as an average of the individual angles of the dominant fracture sets for each bedrock
215   conceptual unit (broken, figured, massive).
216
217   *Geophysical investigations*
218
219   Electrical resistivity tomography and petrophysical models for porosity estimation
220
221   A geophysical survey using electrical resistivity tomography ERT was carried out to provide a
222   catchment-scale conceptual understanding of the bedrock heterogeneity and its hydrogeological
223   significance. ERT was applied along the hillslope transect of the three well clusters using a Syscal Pro
224   72 resistivity meter. As described in Comte *et al*. (2012), the acquisition was carried out with 60
225   electrodes at 5-m unit electrode spacing, subsequently expanded through roll-along. The dipole-
226   dipole (DD) and multi-gradient (mGD) quadripole configurations ran sequentially, ultimately allowing
227   a depth of investigation of 50–60 m (Edwards 1977). After noise removal, DD and mGD apparent
228   resistivity data were jointly inverted using RES2DINV v3.58. The inversion provided a 2D model of
229   specific resistivities in which model regions that are insensitive to the input data were removed
230   using the depth of investigation (DOI) method of Oldenburg & Li (1999). The best model retained for
231   hydrogeological interpretation was obtained for the 5th iteration, giving an absolute error between
232   observed and calculated apparent resistivities of 9.6%.
233   In addition to the structural information provided by the interpretation of spatial resistivity
234   variation, a petrophysical model was applied to the resistivity model in order to derive bedrock
235   porosity. Due to the substantial amount of clay minerals (both primary and secondary) in the
236   psammites and the micaschists, Archie's model (Archie 1942) was not applicable and instead, the
237   Waxman and Smits (1976) model was used. The Waxman and Smits model relates the bulk (specific)
238   resistivity obtained by inversion to the aquifer total porosity (which is the unknown to resolve), the

239   pore water saturation (equal to one below the water table), the rock matrix cementation factor, the
240   groundwater electrical conductivity and temperature, and in addition to Archie's Model, the total
241   rock CEC, which was obtained from mineralogical investigations and natural gamma logs (see section
242   *Aquifer characterisation results*). The model is described in Revil et al. (1998) and was applied to
243   estimate the 2D (hillslope) distribution of total porosity along the transect imaged by ERT. Table 1
244   summarises the values of the parameters used for the different hydrogeological units.
245
246 Magnetic Resonance Sounding
247
248   The magnetic resonance sounding (MRS) method (Legchenko 2013) was applied at 11 points
249 along the ERT transect and close to the borehole clusters (Fig. 1). The MRS surveys provided 1D
250 (vertical) profiles of water content. MRS measurements were performed in two surveys, in 2010 and
251 2016 using the NUMISPLUS and NUMISPOLY instruments, respectively, both developed by IRIS
252 Instruments (France). As described in more detail in Legchenko *et al*. (2017), figure-eight square
253 loops were applied in three configurations: two cable turns of 25-m-side, one turn of 37.5-m-side,
254 and one turn of 50-m-side, with a reference loop in 2016 to improve the signal to noise ratio, which
255 is typically low in fractured rock environments, due to a low water content. Eight out of the 11 MRS
256 soundings had acceptable signal-to-noise ratios; the remaining three are not considered in this work.
257 1D inversion of MRS data was carried out using the SAMOVAR software package. It used the
258 Tikhonov regularization method (Legchenko & Shushakov 1998) and the uncertainty in the inversion
259 results was examined applying Monte-Carlo simulations (Legchenko *et al*. 2017). Geological
260 interpretation of MRS results was performed taking into account the thicknesses of the aquifer units
261 (broken and fissured zone) identified with ERT as structural constraints.
262
263 Estimation of aquifer storage parametres from ERT porosity and MRS water content
264
265   ERT porosity and MRS water content were used to derive aquifer specific yield Sy and effective
266 porosity n_e subsequently used for recharge estimation, and numerical groundwater modelling,
267 respectively. By definition, n_e is the interconnected porosity controlling groundwater mass transport
268 and residence times. Also by definition, Sy, also called drainage porosity, is the mobile pore water
269 not retained by capillarity forces and controls water table fluctuations in unconfined aquifers.
270   In fractured rocks, where porosity is mostly the result of the opening of fractures and foliation
271 planes by (groundwater-aided) weathering, the occurrence of closed (unconnected) pore space is
272 limited (Singhal & Gupta 2010). This implies that total porosity, obtained from ERT, can be
273 considered a close estimate of the effective porosity n_e, which was our assumption for subsequent
274 modelling.
275   The MRS water content is commonly reported (Lubczynski & Roy 2004) as being correlated with,
276 and representing an intermediary between, the drainage porosity Sy (mobile pore water non
277 retained by capillarity forces) and the effective porosity n_e (immobile and mobile interconnected
278 pore water). Recent studies carried out in low porosity fractured environments (Vouillamoz *et al*.
279 2012, 2014) have reported MRS water content values linearly correlated to, although higher than Sy
280 (within a factor 2) estimated through pumping tests. Consequently, for subsequent recharge
281 calculations we have taken Sy at half (0.5 times) the measured MRS water content.
282
283 *Recharge estimations*
284
285   Recharge values were calculated with the water table fluctuation method applicable to recharge
286 estimation in unconfined aquifers (Healy & Cook 2002). The method requires water table time-series
287 as well as well as values of the specific yield at depth where the water table fluctuates. We used the
288 piezometric fluctuations in the shallowest boreholes (GO1T, GO2T and GO3SS) as reported in Cai &
289 Ofterdinger (2016) for the period 2010-2012. For the specific yield, we used the MRS derived values

290 obtained at the approximated depth of the water table (see previous Section) from the MRS
291 soundings nearest to the boreholes; MRS1 and MRS2 for GO1T, MRS4 and MRS5 for GO2T, and
292 MRS8 for GO3SS.
293
294 **Aquifer characterisation results**
295
296 *Aquifer structure and weathering*
297
298 Fracture analysis
299
300   Measurements of hydraulically active fracture from both outcrops and boreholes at the site
301 showed dominant meso-scale (millimetre to metre) fracture occurrences and orientations which
302 correlate with established past tectonic regimes in Ireland (Fig. 3). Two dominant hydraulically active
303 fracture sets were identified: a dominant set with fractures oriented E-W to NE-SW with a dip angle
304 of about 60-80° S to SE; and a less frequent set with fractures also oriented E-W to NE-SW but with a
305 dip angle of about 60-90° N to NW. The dominant fracture set may be attributed to the strike-slip
306 regional fracturing associated with Alpine compression during the Palaeocene, whereas the second
307 set may be attributed to the compressive fabric of the Neo-Proterozoic to late Carboniferous
308 orogenies (Grampian, Caledonian and Variscan), which also characterise the regional-scale
309 lineaments (Fig. 1) and Lower Carboniferous normal faults (Worthington & Walsh 2011), reactivated
310 by the Alpine strike-slip regime (Cooper *et al*. 2012). The most frequently recorded fracture set is
311 oriented WNW–ESE with a low dip angle of 35 ° NNE corresponding to the highly weathered
312 Dalradian schistosity plane (see below). However, this set does not appear to be clearly associated
313 with hydraulic activity in boreholes and therefore may only play a role in the uppermost levels of the
314 aquifer (broken bedrock and possibly the upper part of the fissured bedrock) for which hydraulic
315 activity in boreholes is difficult to record due to their shallow depths and denser
316 weathering/pervasive fracturing.
317   At macro-scale (catchment and regional scale, i.e. 100 m to km; Fig. 1b), cartographic lineaments
318 attributed to glacial erosion preferentially affecting regional geological boundaries and deep
319 weathering corridors were found to be typically associated with the measured pre-Alpine NE–SW
320 trend (Comte *et al*. 2012).
321
322 Mineral analysis
323
324   Mineralogical investigations reveal that phyllosilicate minerals are dominated by muscovite and
325 chlorite (primary) and illite and montmorillonite (secondary clays produced by weathering of chlorite
326 and muscovite) (Caulfield *et al*. 2014). Major non-clay minerals comprise quartz and feldspar.
327   Relative proportions of clay minerals versus the total clay mass fraction are presented in Table 2.
328 The massive (unweathered) bedrock encountered in the deep boreholes was found to contain
329 negligible secondary clays, with only primary chlorite and muscovite observed. The fissured zone in
330 boreholes GO2 and GO3 contained an approx. equal mixture of illite and montmorillonite with lesser
331 amounts of chlorite and muscovite, and in GO1, relatively even quantities of the four minerals. This
332 suggests a moderate weathering of the fissured zone primary clays in GO1, whilst in GO2 and GO3,
333 they have undergone major weathering as evidenced by the almost complete absence of chlorite.
334 Over 80% of clays in the broken zone were muscovite and the remaining 20% approx. equal
335 proportions of illite and montmorillonite. Because weathering is most active in the broken zone, it
336 was concluded that secondary clays are transported in suspension downward from the broken zone
337 and redeposited in the underlying fissured zone (Comte *et al*. 2012; Caulfield *et al*. 2014).
338   Table 2 also details the total clay mass fraction as derived from natural gamma ray logs. The
339 relative proportions of clay minerals and the total clay mass fraction allowed calculation of the total
340 CEC of the different aquifer units using the model of Revil *et al*. (1998). The total clay content of the

341 different aquifer units (broken, fissured and massive bedrock) was not significantly different;
342 however due to significant differences in clay mineralogy, the resulting CEC is different. The fissure
343 bedrock, with a higher proportion of illite and montmorillonite (secondary weathering clays
344 characterised by high CECs) consistently produced the highest bulk CEC values. The massive bedrock
345 dominated by muscovite and chlorite (primary clays characterised by low CEC values) produced the
346 lowest bulk CEC. This CEC distribution is relevant to the interpretation of ERT results and application
347 of the petrophysical models in which it is a key input parameter.
348
349 Geophysical structure
350
351   Results of the ERT investigations provide cross-sectional variations of electrical resistivity along
352 the borehole hillslope transect (Figure 4), revealing a high degree of aquifer heterogeneity. As
353 electrical resistivity is primarily controlled by porosity (fracture porosity in the present context), clay
354 content and mineralogy, its spatial variations can be interpreted as reflecting changes in lithology,
355 pore water saturation, open fracture density and weathering intensity. Resistivity values range from
356 about 100 ohm.m to just under 10 000 ohm.m, i.e. three orders of magnitude. Highest resistivities
357 (>> 1000 ohm.m) were observed at the base of the transect and reflect the massive micaschist unit
358 beneath the weathered front, characterised by a low density closed fractures and small quantities of
359 secondary weathering clays. Some equally high resistivity values were also obtained in the very
360 shallow subsurface in the higher elevation part of the profile. Correlations with the depth of the
361 water table in borehole cluster GO1 and observed spring lines at its base suggested that this
362 uppermost, high resistivity unit corresponds to unsaturated, clay-poor psammite-schist. The lowest
363 resistivity values (<500 ohm.m) were obtained at a relatively shallow depth in the flood plain and
364 corresponded to the clay-till and alluvium overburden. Intermediate resistivity values (500-2500
365 ohm.m) were observed throughout the whole transect at shallow to intermediate depths (0 to about
366 50 m below surface) and characterised the heterogeneous weathered/fractured schists (broken and
367 fissured bedrock). The relatively continuous unit with values ranging ~300-1000 ohm.m overlying the
368 massive bedrock are interpreted as fissured bedrock characterised by a high density of open
369 fractures possibly filled with high-CEC weathering clays as suggested by the clay mineralogy. This
370 fissured layer was particularly deep at three locations along the transect; at the following horizontal
371 distances from NW end of the profile of X=400-500 m, 750-850 m and 1100-1300 m. Since they
372 correlate well with the regional Grampian lineaments (Fig. 1), these locations are interpreted as
373 deep fractured zones that facilitate deep weathering. At these three locations a slightly more
374 resistant layer was observed overlying the fissured layer, with resistivities in the range of 500-2500
375 ohm.m. This unit is interpreted as the broken schists (transition zone) where the weathered clays
376 have been leached and transported to the underlying fissured zone.
377
378 *Flow properties*
379
380   Pumping and recovery tests in every borehole provided estimates of (equivalent isotropic)
381 hydraulic conductivities K for bedrock and overburden (Table 3). A clear trend of decreasing
382 hydraulic conductivity with depth is observed. The broken bedrock (transition zone) displayed mean
383 values close to 10^{-1} m/d, the fissured bedrock close to 10^{-2} m/d with large variability of over two
384 orders of magnitude and the massive (deep) bedrock around 6×10^{-3} m/d. The overburden (glacio-
385 fluvial and alluvium deposits) present in the valley floor displayed much higher mean K values of ~9
386 m/d. These values partly agree with values from previous hydraulic tests by Moe *et al*. (2010). These
387 authors obtained much higher mean K for the broken bedrock due to one very high value (of about 7
388 m/d) obtained in the valley floor at GO3, which may be representative of the interface between the
389 overburden glacio-fluvial deposits and the bedrock. They also provided values for the deep massive
390 bedrock that are similar to those in the overlying fissured (shallow) bedrock.

391   *Kmax*, *Kmin* and the anisotropy angles (angle of *Kmax* to the horizontal plane, in °) in the 2D
392   vertical plane of the studied transect were further derived based on the measured orientation of the
393   dominant, hydraulically active fracture sets (see previous Section); a primary set ~70° dipping SSE
394   and secondary set ~75° dipping NNW, and another set ~35° dipping NNW which is not clearly
395   hydraulically active at large depths, but is probably active in the weathered near-surface. The
396   anisotropy ratio *Kmin*/*Kmax* (unitless) was assumed to decrease with depth from 0.5 to 0.1 (see
397   Section *Methods*). The calculated anisotropy angle increased with depth from a relatively low angle
398   in the broken bedrock as a result of the equal contribution of the three fracture sets (75° NW) to a
399   dominant steep angle in the deep bedrock (70° SE, parallel to dominant hydraulically active Variscan-
400   Alpine fabrics). Fig. 5 plots the values of *Kmin*, *Kmax* along with the previous equivalent isotropic *K*
401   estimates (Moe *et al*. 2010; Comte *et al*. 2012). The values of *Kmax* were close to the values
402   obtained from hydraulic tests, which were assumed to preferentially mobilise groundwater from the
403   fractures responsible for *Kmax* (direction of maximum anisotropy).
404
405   *Storage properties*
406
407   Quantitative information on the heterogeneity of aquifer storage properties was provided by the
408   joint analysis of hydraulic test results and geophysical data (MRS and ERT). Hydraulic test results are
409   limited to single estimates of specific yield (*Sy*). Moreover, *Sy* values obtained from measurements in
410   pumped wells in absence of observation wells are usually inaccurate due to possible well bore
411   storage effects. However they did provide indicative orders of magnitude as a guide, with broken
412   bedrock displaying *Sy* values around 3-5 %, fissured bedrock of about 0.1 % and massive bedrock
413   around 0.001 %, i.e. over an order of magnitude decrease between each layer with increasing depth.
414   Geophysical data provided higher resolution spatial information on the variability of storage
415   properties. MRS, despite an instrumental sensitivity that currently does not reliably quantify less
416   than 1 % water content, detected appreciable quantities of water above 2% in the central and low
417   part of the transect (Fig. 6). The highest water contents were detected at MRS8 in the valley floor
418   with values between 2 and 6 % at shallow depths (0-25 m) corresponding to the occurrence of the
419   relatively porous overburden materials and the broken bedrock. Similar water content values were
420   also obtained at MRS4, upslope of GO2, at depths (2-15 m) consistent with the area of deep
421   weathering identified by ERT (X=400-600 m on Fig. 4) and characterised by significant deepening of
422   the broken bedrock layer. In the upper part of the transect around GO1, no appreciable water
423   content was detected by MRS suggesting water content < 1 %. This is also the case for the two
424   soundings carried out between GO2 and the valley floor. Overall, the MRS results show relatively
425   good agreement with the depth delineation of the broken bedrock and overburden layers from ERT
426   (Fig. 6 and 7a,b). For the overburden in the valley floor, MRS water content values of approx. 5-6 %
427   were obtained while the broken bedrock (transition zone) yielded values of 2-4 %. At depth below
428   the base of the broken layer (as delineated with ERT), MRS mostly provided either water content
429   values below the normal limit of detection of the methods (1 % water content) or values with high
430   inversion uncertainty. This suggests that the fissured and massive bedrock had water content values
431   < 1 %. Note that the broken bedrock, which is likely present in the upper part of the transect was
432   mostly unsaturated in the summer (dry) conditions when both ERT and MRS surveys were
433   undertaken.
434   The Waxman and Smits model (Fig. 7c), provided spatial variations of (effective) porosities
435   consistent with MRS results, and porosity values of about half the MRS water contents. Values
436   ranging from 3-7 % were obtained in the overburden/broken bedrock of the valley floor while the
437   broken layer of the mid and upper part of the transect displayed values ranging from 1 to 3 %,
438   decreasing with distance to valley floor. For the fissured layer, we obtained values between 1 %
439   beneath the valley floor to less than 0.1 % in the upper part of the transect, with a relatively
440   progressive decrease from valley bottom to hilltop. Porosities lower than 0.03 % were obtained in
441   the massive, unweathered bedrock layer. As a comparison, Archie's model (not presented here),

442   which is applicable in clay-free materials, provided much higher, unrealistic porosity values of about
443   an order of magnitude (i.e. about ten times) higher, ranging 1 to 40 %. This confirmed that Archie's
444   model is not applicable in this type of environment due to significant clay content.
445   The slightly lower (effective) porosities values obtained from the Waxman and Smits model as
446   compared to the MRS water content values, of approximately a factor of two, are consistent with
447   the findings from Vouillamoz *et al*. (2012, 2014) who reported similar difference factors in low
448   porosity (< 3 %) clay-rich bedrock aquifers. This supports the assumption, used for subsequent
449   modelling of residence times, that bedrock effective porosities may reasonably be assumed as equal
450   to Waxman and Smits porosities.
451
452   *Aquifer recharge*
453
454   Application of the water table fluctuation using *Sy* values derived from MRS provided recharge
455   values that vary along the hillslope (Table 4), from an average of 163 mm/y in the hillslope to an
456   average of 287 mm/y in the valley bottom, which correspond to about 10% and 20% or the rainfall,
457   respectively. These values are higher than previous values reported by Cai & Ofterdinger (2016) due
458   to estimated *Sy* values higher than the literature values used by previous authors.
459
460
461   **Data integration and numerical groundwater modelling**
462
463   *Methods*
464
465   A 2D numerical groundwater model (equivalent porous medium EPM) was constructed in line
466   with the ERT transect in order to assess the influence of the structural heterogeneity, i.e. the spatial
467   variations in flow (permeability, anisotropy) and storage (porosity) properties on groundwater flow
468   paths and residence time. EPM models are commonly used for studying groundwater dynamics in
469   fractured bedrock aquifers at catchment and hillslope-scale (Ball *et al*. 2014; Welch & Allen 2014;
470   Kolbe *et al*. 2016). EPM models use integrated hydraulic properties data (hydraulic conductivities,
471   storativities) from hydraulic test solutions and anisotropy analysis (which are also EPM models).
472   They are also a lot less computationally expensive than discrete fracture network (DFN) models for
473   which the current hillslope-scale knowledge on the actual distribution and properties (length,
474   aperture, roughness) of fracture networks is insufficient for DFN model application.
475   We used the finite element code FEFLOW v6.2. The model domain was 2D vertical (cross section;
476   Fig. 8) with a length slightly shorter than the ERT transect (1200 m; the ERT region south of the river
477   was not included). The ground surface was obtained from the DEM and therefore identical to the
478   ERT profile. The maximum elevation (NW of transect) was 183 m and the minimum river elevation
479   (SW of transect) was 31.5 m, i.e. the elevation of the river. The base of the model was fixed at -50 m
480   relative to mean sea level. The mesh comprised 5366 triangular elements and 2974 nodes.
481   The model domain was structured in five layers: alluvium (only present in the floodplain), broken
482   bedrock, fissured bedrock, massive bedrock, and a hypothetical very low conductivity/porosity
483   bottom layer (Figure 8), within which homogeneous hydrogeological parameters were applied. Two
484   alternative numerical models were applied using different levels of hydrogeological knowledge of
485   the site (aquifer structure, hydraulic properties, and recharge). Model 1 used the information
486   obtained from boreholes only. It considered a uniform layered structure defined from lateral
487   interpolation of the hydrogeological units as identified in boreholes and initially interpreted by Moe
488   *et al*. (2010) prior to extensive deployment of geophysical surveys. This model represents the
489   common, most simple catchment/regional scale conceptualisation of basement aquifers (Fig. 8a).
490   Model 2 incorporated the additional knowledge obtained from the interpretation of geophysical
491   surveys (Fig. 8b). Comparing the two models aimed at illustrating the added value provided by the
492   geophysical data. Details of the set up of both models were as follows.

493
494   **Model 1** considered a tabular spatial distribution of the different aquifer units that mimics the
495   topography (Figure 8a). Recharge values were based on borehole-based estimates by Cai &
496   Ofterdinger (2016). Model hydraulic conductivities and porosities were assigned from layer-specific
497   hydraulic test results from Moe et al. (2010) and Comte *et al*. (2012), respectively (Table 5). Effective
498   porosities, used for residence time calculations, were assumed to be equal to the specific yield
499   values (*Sy*) from borehole data. As Model 1 initially provided a poor fit to observed groundwater
500   heads, a recalibration had to be performed through increasing recharge (x5) and decreasing
501   hydraulic conductivities (/5).
502
503   **Model 2** was based on the geometry of the different aquifer units from the interpretation of the
504   geophysical data (ERT and MRS). Recharge values were the new values calculated with the water
505   table fluctuation method using the specific yield data derived from the MRS surveys (see Section
506   *Aquifer characterisation*). Hydraulic conductivities *K* (Table 5) were applied as anisotropic and
507   assigned from joint interpretation of revised hydraulic test data Comte *et al*. (2012), geophysical
508   data and fracture analyses (see Section *Aquifer characterisation*). Effective porosities (Table 5) were
509   assigned using the porosity values obtained from joint application of ERT and MRS (Figure 7 and
510   Table 5).
511
512   Both models were assigned values of longitudinal and transversal dispersivity of 30 and 3 m
513   respectively, as typically reported for fractured aquifers for the scale of this study (hundreds of m to
514   km-scale flow paths; Neuman 2005; Schulze-Makuch 2005; Zhou *et al*. 2007). With regard to the
515   boundary conditions other than the recharge described above, both models also computed the top
516   surface as a seepage face, with recharge (entering flux) switching automatically to discharge (exiting
517   flux) during simulations when the water table was equal or higher than the top surface. Additionally,
518   the river was applied as a constant head of 31.5 m, which is the average observed river level. In
519   terms of groundwater ages, water entering from recharge was assigned a constant age of 0 years.
520   Models were run in transient flow and age conditions with initial heads equal to the topographic
521   elevation and initial ages of 0 years, until reaching a dynamic steady state. Flow and groundwater
522   age were solved simultaneously. Groundwater age simulations in FEFLOW are treated as dissolved
523   transport and account for the applied values of effective porosities and dispersivities. This, contrary
524   to isochrone calculations on flow paths (streamlines), allows for water dispersion and mixing of
525   groundwater ages. Flow path simulations were run on simulated flow fields to highlight average flow
526   paths from recharge (top surface) to discharge points (river and seepage areas).
527
528   *Numerical modelling results*
529
530   Models evaluation
531
532   The goodness-of-fit of the different models, i.e. the discrepancy between predicted and observed
533   heads was assessed through root-mean-square error (RMSE) calculations. Model 1, which computed
534   previously published values of hydraulic properties (Moe *et al*. 2010) and recharge (Cai &
535   Ofterdinger 2016) initially failed to reproduce hydraulic heads that fit the observed head in the
536   boreholes. Calculated head values were significantly lower than observed, of up to 125 m difference
537   at GO1 (uphill), due to either underestimation of the recharge or overestimation of the aquifer
538   hydraulic conductivities, but close to observations downhill due to the constraint by the river fixed
539   head. Across the whole transect this model produced a high total RMSE of 71.6 m. The recalibration
540   of Model 1, through increasing the recharge and decreasing *K* both by a factor five, produced a
541   reasonable fit with a RMSE of 3.7 m. Models 2 directly reproduced reasonably well the hydraulic
542   heads observed in the boreholes GO1, GO2 and GO3 with a RMSE of 4.0 m. For Model 2 however,
543   the simulated heads in the deep GO1 and GO2 boreholes were somewhat higher than those

544 observed. Because these two boreholes are within or close to deep weathered/fractured zones (as
545 identified by geophysics), a 3D model allowing deep and lateral drainage would be expected to
546 correct for this mismatch by lowering heads in the deep units. The model comparison demonstrates
547 that both Model 1 (final recalibrated version) and Model 2 equally honour the observed heads,
548 however only Model 2 also honours the observed aquifer properties, structure and recharge values.

549 Simulation of groundwater fluxes, flow paths and residence time distributions
550

551 For both Model 1 and Model 2, Darcy's fluxes were highest in the broken bedrock and decreased
552 with depth (Fig. 9a,d). The deep weathered/fractured zones identified by geophysics and computed
553 in Model 2 allowed for thicker areas of high flux (Fig. 9d), especially in the vicinity of these zones (X
554 300-600 m; 750-850 m; 110-1300 m). In terms of budget (Fig. 10), in the case of Model 1 almost 80
555 % of the flow rate in the aquifer, originating from the recharge, transited through the broken
556 bedrock layer (transition zone) and fissured layer (shallow zone), with over 60% in the broken
557 bedrock only. The proportion was lower for Model 2, with about 70% flowing through broken and
558 fissured bedrock and about 50% through the broken bedrock only. This suggests that overall
559 hydrogeological heterogeneity favours deeper groundwater flow in the fissured and massive
560 bedrock (< 20 % for Model 1 vs. about 25 % for Model 2).
561 This is further confirmed by the average flow path (streamlines) simulations (Fig. 9b,e). In the
562 case of Model 1, most flow paths were sub-horizontal and restricted to the shallow broken layer (Fig.
563 9b). A limited number of flowlines travel through the fissured and massive layers. For Model 2,
564 which incorporated lateral variations in the thickness of the aquifer layers, flow paths were more
565 evenly distributed with depth, with higher contributions from the fissured and massive layers (Fig.
566 9e). They were also characterised by undulations as a result of lateral variations of weathering
567 thicknesses and the anisotropy of conductivity with an increased vertical component to the
568 groundwater flow. In detail, Model 2 simulations showed sub-vertical or oblique groundwater flow
569 from recharge locations where weathering/fracturing is poorly developed. In locations with
570 extensive weathering/fracturing, groundwater directions changed upwards suggesting that these
571 locations may act as drainage structures at catchment and regional scale. These model regions were
572 also associated with groundwater discharge through seepage, which agree with the spring lines
573 locations observed in the field (Fig. 4). Seepage appeared to occur specifically in areas where the two
574 following conditions are met: (1) upwelling groundwater flow associated to decrease in thickness of
575 the broken bedrock on the downgradient side of deep weathered/fractured 'channels' and (2)
576 presence of topographic low also associated to less competent bedrock in these zones. In contrast
577 the absence of deep weathering zones in Model 1 resulted in higher and more evenly spread
578 seepage along the hillslope.
579 Groundwater age simulations for the two models (Fig. 9c,f and Fig. 11) provided ages increasing
580 both laterally from hill top to the valley and with depth. Youngest groundwater was obtained in
581 GO1T and GO3SS and oldest in GO3S, GO3D and GO2D (Fig. 11). Model 1 and Model 2 both resulted
582 in simulated ages less than about 10 years and 50 years, respectively, in boreholes and seepages
583 areas. When compared to Model 1, which did not incorporate lateral heterogeneity, Models 2
584 showed greater age mixing with depth whereas the former produced steeper age gradient with
585 depth in the upper aquifer. Model 2 ages are consistent with independent Tritium data (Pilatova
586 2013) that showed (1) Tritium concentrations in boreholes within the range 2.5-17.6 TU reflecting a
587 mixture of sub-modern water (< 1TU; prior 1952) and modern water (5-15+ TU, i.e. < 5 to 10 years)
588 (Figure 11), (2) decreasing Tritium values with depth reflecting larger component of older waters
589 with depth, (3) highest Tritium values (>14 TU) in the upper bedrock at GO1T well (X=~100 m) and
590 GO2S well (X=~600 m) reflecting high proportion of young water associated to recharge as well as
591 descending to sub-horizontal groundwater flow and (4) lowest Tritium values (2.5 TU) encountered
592 at the deep GO3D well (X=~1200 m) reflecting larger component of older upwelling groundwater.
593 The distribution of residence times obtained for Model 2, the best parameterised model
594 accounting for the geophysical heterogeneity, is also broadly consistent with previous catchment- or

595 hillslope-scale studies in fractured hard rock aquifers. Robins & Smedley (1994) reported modern
596 groundwater tritium ages in the fractured basement of Jersey. Jaunat *et al*. (2012) reported CFC-SF6
597 residence times lower than 50 years in weathered/fractured gneiss of the French Basque Country for
598 similar flow path lengths. Banks *et al*. (2009) reported CFC ages of less than 40 years in a hillslope
599 transect underlain by weathered/fractured metasediments. Lapworth *et al*. (2013) reported CFC-
600 SF6-3H mean residence times of 32-65 years in deeply weathered catchments of the West African
601 basement. Kolbe *et al*. (2016) modelled mean transit times of 40 years in a granite-gneiss catchment
602 of ~10 km-long with similar mean flow path lengths of ~300 m. The modelling results also
603 corroborate recent findings by Ameli *et al.* (2016) who showed the major impact of subsurface
604 heterogeneity on groundwater residence time distribution in a well-studied hillslope transect in
605 glacial till in Sweden.
606
607
608 **General discussion**
609
610 *Study implications for groundwater resilience to climate change and contaminants, and*
611 *catchment management approaches*
612
613   The results indicate that overall low and depth-decreasing porosities, together with high
614 hydraulic gradients, give relatively short residence times for groundwater from recharge to seepage
615 or river discharge. In the upper bedrock (broken bedrock/transition zone; 1 to 30 m thick), where
616 over 50% of groundwater flow occurs, models results suggest groundwater flow paths of between
617 10-100 m long and groundwater ages of < 1 year. This implies that groundwater in this aquifer unit is
618 sensitive to both weather seasonality and extreme events (winter/summer recharge condition and
619 drought/floods). This groundwater mostly contributes to diffuse seepage, which is then collected by
620 agricultural drains. As such, point and diffuse contaminants in groundwater are expected to affect
621 surface water quickly, on timescales of days to months. In the deeper bedrock (fissured/shallow and
622 massive/deep bedrock; depths higher than 10-50 m), model results yield longer flow paths (100-
623 1000 m) and older groundwater ages (from one year to several decades). This implies higher
624 groundwater resilience to extreme weather conditions, seasonality and incidental contaminant
625 exposures, but not to long-term (multi-decadal) climate change and persistent contamination, such
626 as (i) changes in recharge due to long-term changes in rainfall and evapotranspiration and (ii) diffuse
627 (e.g. agricultural nutrients) contamination. As these deeper bedrock units mostly contribute to river
628 flow as well as the most significant seepages areas/drains, the surface water network at base flow
629 (i.e. when mostly supported by groundwater) is also expected to be more vulnerable to long-term
630 climate change and contamination.
631   Model comparison (Model 1 vs. Model 2) further highlights the importance of adequately
632 accounting for aquifer heterogeneity when using models to predict the response of
633 weathered/fractured rock catchments to climate and land use change as well as contaminations.
634 Using information from borehole observations only, which does not allow for adequately capturing
635 spatial variations in weathering/fracturing, leads to underestimation of the contribution of deep
636 aquifer units to catchment water balance and discharge to river/surface water bodies. This also
637 leads to underestimating groundwater residence times and exaggerating both ground and surface
638 water sensitivity to climate variability and contaminations. In contrast, better accounting for aquifer
639 heterogeneity as revealed here by geophysical surveys, results in higher resilience of groundwater
640 resources to climate variability and surface contaminations. This is of importance when applying
641 groundwater models with the aim of accurately informing short to long-term catchment
642 management and policy.
643
644
645

Study limitations and implications for residence time distributions

The hydrogeophysical and numerical modelling works conducted in this study reveal the major role played by hydrogeological heterogeneities on groundwater flowpaths and transit time distributions at 2D hillslope scale providing important insights into catchment scale groundwater processes in weathered/fractured aquifers. The methodology however has some limitations with respect to accurately representing 3D heterogeneities and their influence on flow and transit times at smaller (i.e. borehole) or larger (i.e. catchment or region). Specifically, the hillslope characterisation and modelling work conducted do not represent; (1) three-dimensional groundwater flow such as lateral or deep drainage due to deep weathering structures possibly significant at the catchment/regional scale; (2) individual fracture networks and associated fracture flow processes; (3) accurate 2D/3D clay distribution and cementation factor; (4) uncertainty in estimates of hydrogeological porosity from geophysical (ERT and MRS) porosity; (5) temporal variability in recharge; (6) flow processes in the unsaturated zone above the water table.

With regards to the two-dimensionality of the models, it may be expected that some groundwater flow at the catchment scale may take place laterally to the 2D transects especially (i) in deep weathering furrows such as these detected by geophysics at about 300-600m, 750-850m and 110-1300m; (ii) in more local preferential flow paths along the NE-SW fractured systems. Not accounting for these 3D processes, the current modelling approach is likely to lead to underestimate deep groundwater flow as well as mixing and resulting groundwater ages, and overestimate seepage (along the hillslope). Full 3D geophysical (acquisition and inversion) and numerical modelling approaches are recommended in basement catchments where strong 3D heterogeneity is expected. The expected increased accuracy is however at the cost of much higher requirement in terms of acquisition and modelling time and resource, including computational.

Increased accuracy in modelling results may also be obtained by implementing discrete fractured network (DFN) modelling approaches. The structural and geophysical data may be used to support the computation of fracture orientation and density, which would allow direct computation of fracture permeability and aperture. A DFN approach requires implementation of computationally expensive 3D models.

Application of ERT to derive porosities requires information on spatial variations of bedrock clay content and clay mineralogy. Direct and high resolution 3D characterisation of clay properties through sampling/coring is challenging, but such resolution may be achieved indirectly through use of alternative geophysical methods such as the induced polarisation (IP).

In line with previous works in similar settings, we have assumed that aquifer effective porosity was half the MRS water content and equal to ERT porosity. Should this assumption be erroneous, effective porosity values higher than the ERT total porosity would result in higher groundwater residence times. More research is recommended to constrain the relationship between ERT/MRS porosity and hydrogeological porosities (storativity and effective porosity).

The temporal variability in recharge has not been accounted for and would be required to better understanding seasonality in groundwater contribution to seepage, drains and stream. It may, in addition, enhance groundwater mixing and, therefore groundwater residence times. Similarly, neglecting flow processes in the unsaturated zone primarily result in underestimating groundwater mixing and ages in areas where the unsaturated zone is thicker.

Conclusion

The study highlights the strong control of geological heterogeneities on groundwater flow and residence times in metamorphic rock catchments in temperate regions. It also demonstrates the high value of surface geophysical data and fracture and clay analysis for the parametrisation of numerical groundwater models in complex aquifers.

697   The investigations have revealed a high degree of heterogeneity in the distribution of
698   hydrogeological properties at the hillslope scale. Through 2D equivalent porous media modelling
699   using FEFLOW, it has been shown that the high spatial variation of hydraulic conductivity and
700   porosity results in deeper groundwater flow paths (with an increased in the vertical flow component
701   with depth) as compared to simple layered conceptual models based on borehole data only. They
702   also result in older groundwater ages through enhanced mixing and dispersion caused by
703   heterogeneities and anisotropies of hydraulic conductivity. Groundwater ages along the hillslope
704   were simulated to be of modern ages, i.e. less than 50 years, consistent with available Tritium data.
705   The integrated approach presented, using both borehole and surface geophysical surveys, is
706   shown to help parametrise numerical groundwater models that honour the observed data without
707   requiring significant parameter recalibration. Such robustly parameterised models offer
708   straightforward application in catchment water management, to investigate in detail the
709   contribution of groundwater to the catchment hydrological function, as well as the impact of climate
710   change and contaminants on groundwater.
711   The results presented here suggest that the uppermost weathered/broken part of the aquifer,
712   which is a major contributor to hillslope discharge, is sensitive to extreme hydrological events and
713   seasonal climate fluctuations as well as point and diffuse contamination. The deeper, less weathered
714   part of the aquifer is a significant contributor to river flow and major hillslope seepage areas and
715   would be more sensitive to long-term (decadal) climate fluctuations and persistent, diffuse
716   contaminants.
717   It is suggested that the 2D steady-state hillslope approach conducted provides only a minimum
718   estimate of groundwater ages at the catchment scale. This is due to underestimation of
719   groundwater mixing favoured by possible 3D structures and seasonal recharge. Full 3D
720   characterisation and modelling approaches, although more expensive in terms of data and
721   computational resources, are required to further improve our understanding of groundwater flow
722   and residence times. Recommendations include: (1) implementation of 3D MRS and ERT surveys and
723   inversion, including 3D characterisation of clay mineralogy through alternative geophysical methods
724   such as IP; (2) resolution and computation of fracture networks and fracture flow; (3) application of
725   transient, variably saturated model for better accounting of mixing and processes in the unsaturated
726   zone; (4) more research on the relationship between geophysical (ERT and MRS) porosity and
727   hydrogeological porosity.
728
729

Acknowledgements

742
743
744

References

Ameli, A.A., Amvrosiadi, N., Grabs, T., Laudon, H., Creed, I.F., McDonnell, J.J. & Bishop, K. 2016. Hillslope permeability architecture controls on subsurface transit time distribution and flow paths, *Journal of Hydrology*, **543**, 17–30, https://doi.org/10.1016/j.jhydrol.2016.04.071

Archie, G.E. 1942. The electrical resistivity log as an aid in determining some reservoir characteristics, *Transactions of the AIME*, **146**(01), 54–62, https://doi.org/10.2118/942054-G

Ball, L.B., Caine, J.S. & Ge, S. 2014. Controls on groundwater flow in a semiarid folded and faulted intermountain basin, *Water Resources Research*, **50**(8), 6788–6809, http://dx.doi.org/10.1002/2013WR014451

Baltassat, J.M., Legchenko, A., Ambroise, B., Mathieu, F., Lachassagne, P., Wyns, R., Mercier, J.L. & Schott, J.J. 2005. Magnetic resonance sounding (MRS) and resistivity characterisation of a mountain hard rock aquifer: the Ringelbach Catchment, Vosges Massif, France, *Near Surface Geophysics*, **3**(4), 267–274

Banks, E.W., Simmons, C.T., Love, A.J., Cranswick, R., Werner, A.D., Bestland, E.A., Wood, M. & Wilson, T. 2009. Fractured bedrock and saprolite hydrogeologic controls on groundwater/surface-water interaction: a conceptual model (Australia), *Hydrogeology Journal*, **17**(8), 1969–1989, https://doi.org/10.1007/s10040-009-0490-7

Boucher, M., Favreau, G., Vouillamoz, J.M., Nazoumou, Y. & Legchenko, A. 2009. Estimating specific yield and transmissivity with magnetic resonance sounding in an unconfined sandstone aquifer (Niger), *Hydrogeology Journal*, **17**(7), 1805–1815, https://doi.org/10.1007/s10040-009-0447-x

Cai, Z. & Ofterdinger, U. 2016. Analysis of groundwater-level response to rainfall and estimation of annual recharge in fractured hard rock aquifers, NW Ireland, *Journal of Hydrology*, **535**, 71–84, https://doi.org/10.1016/j.jhydrol.2016.01.066

Carroll, D. 1959. Ion exchange in clays and other minerals, *Geological Society of America Bulletin*, **70**(6), 749–779, https://doi.org/10.1130/0016-7606(1959)70[749:IEICAO]2.0.CO;2

Cassidy, R., Comte, J.C., Nitsche, J., Wilson, C., Flynn, R. & Ofterdinger, U. 2014. Combining multi-scale geophysical techniques for robust hydro-structural characterisation in catchments underlain by hard rock in post-glacial regions, *Journal of hydrology*, **517**, 715–731, https://doi.org/10.1016/j.jhydrol.2014.06.004

Caulfield, J., Chelliah, M., Comte, J.C., Cassidy, R. & Flynn, R. 2014. Integrating petrography, mineralogy and hydrochemistry to constrain the influence and distribution of groundwater contributions to baseflow in poorly productive aquifers: Insights from Gortinlieve catchment, Co. Donegal, NW Ireland, *Science of the Total Environment*, **500**, 224–234, https://doi.org/10.1016/j.scitotenv.2014.08.105

Chandra, S., Dewandel, B., Dutta, S. & Ahmed, S. 2010. Geophysical model of geological discontinuities in a granitic aquifer: Analyzing small scale variability of electrical resistivity for groundwater occurrences, *Journal of Applied Geophysics*, **71**(4), 137–148, https://doi.org/10.1016/j.jappgeo.2010.06.003

795   Chew, D.M. 2009. Grampian orogeny. *In*: Holland, C.H. & Sanders, I.S. (eds) *The geology of Ireland*.
796   Dunedin, Edinburgh, 69–93.
797
798   Comte, J.C., Cassidy, R., Nitsche, J., Ofterdinger, U., Pilatova, K. & Flynn, R. 2012. The typology of Irish
799   hard-rock aquifers based on an integrated hydrogeological and geophysical approach, *Hydrogeology*
800   *Journal*, **20**(8), 1569–1588, https://doi.org/10.1007/s10040-012-0884-9
801
802   Cooper, M.R., Anderson, H., Walsh, J.J., Van Dam, C.L., Young, M.E., Earls, G. & Walker, A. 2012.
803   Palaeogene Alpine tectonics and Icelandic plume-related magmatism and deformation in Northern
804   Ireland, *Journal of the Geological Society*, **169**(1), 29–36, https://doi.org/10.1144/0016-76492010-
805   182
806
807   Crain, E.R. (eds) 2000. *Crain's petrophysical handbook*. Spectrum.
808
809   Daly, D., Deakin, J., Craig, M., Mockler, E.M., et al. 2016. Progress in Implementation of the Water
810   Framework Directive in Ireland. International Association of Hydrogeologists (IAH) (Irish Group)
811   Sustaining Ireland's Water Future: The Role of Groundwater, Tullamore, Co. Offaly, Ireland, 12-13
812   April 2016.
813
814   DCCAE 2017. Groundwater, Department of Communications, Climate Action and Environment,
815   Government of Ireland. http://www.dccae.gov.ie/en-ie/natural-resources/topics/Geological-Survey-
816   of-Ireland/groundwater/Pages/Groundwater.aspx
817
818   Day-Lewis, F.D., Slater, L.D., Robinson, J., Johnson, C.D., Terry, N. & Werkema, D. 2017. An overview
819   of geophysical technologies appropriate for characterization and monitoring at fractured-rock sites,
820   *Journal of Environmental Management*, **204**, 709–720,
821   https://doi.org/10.1016/j.jenvman.2017.04.033
822
823   De Marsily, G., Delay, F., Goncalves, J., Renard, P., Teles, V. & Violette, S. 2005. Dealing with spatial
824   heterogeneity, *Hydrogeology Journal*, **13**(1), 161–183, https://doi.org/10.1007/s10040-004-0432-3
825
826   Descloitres, M., Ruiz, L., Sekhar, M., Legchenko, A., Braun, J.J., Kumar, M. & Subramanian, S. 2008.
827   Characterization of seasonal local recharge using electrical resistivity tomography and magnetic
828   resonance sounding, *Hydrological Processes*, **22**(3), 384–394, http://dx.doi.org/10.1002/hyp.6608
829
830   Ellis, D.V. & Singer, J.M. 2007. *Well logging for earth scientists*. Dordrecht, Springer.
831
832   EPA 2006. Ireland; Water Framework Directive, Monitoring Programme prepared to meet the
833   requirements of the EU Water Framework Directive (2000/60/EC) and National Regulations
834   implementing the Water Framework Directive (S.I. No. 722 of 2003) and National Regulations
835   implementing the Nitrates Directive (S.I. No. 788 of 2005), Environmental Protection Agency, Co.
836   Wexford, Wexford, Ireland
837
838   Francés, A.P., Lubczynski, M.W., Roy, J., Santos, F.A. & Ardekani, M.R.M. 2014. Hydrogeophysics and
839   remote sensing for the design of hydrogeological conceptual models in hard rocks–Sardón
840   catchment (Spain), *Journal of Applied Geophysics*, **110**, 63–81,
841   https://doi.org/10.1016/j.jappgeo.2014.08.015
842
843   Gillespie, M.R., Kemp, S.J., Vickers, B.P., Waters, C. & Gowing, C.J. 2001. *Cation-exchange capacity*
844   *(CEC) of selected lithologies from England, Wales and Scotland*, SEPA R&D Technical Report, **P2-**
845   **222/TR**.

846

847 Hartmann, D.J. & Beaumont, E.A. 1999. *Predicting reservoir system quality and performance.*
848 *Exploring for oil and gas traps*. AAPG Treatise of Petroleum Geology, Handbook of Petroleum
849 Geology.

850

851 Healy, R.W. & Cook, P.G. 2002. Using groundwater levels to estimate recharge, *Hydrogeology*
852 *journal*, **10**(1), 91–109, https://doi.org/10.1007/s10040-001-0178-0

853

854 Henn, F., Durand, C., Cerepi, A., Brosse, E. & Giuntini, J.C. 2007. DC conductivity, cationic exchange
855 capacity, and specific surface area related to chemical composition of pore lining chlorites, *Journal of*
856 *colloid and interface science*, **311**(2), 571–578, https://doi.org/10.1016/j.jcis.2007.02.062

857

858 Hertrich, M., Green, A.G., Braun, M. & Yaramanci, U. 2009. High-resolution surface NMR tomography
859 of shallow aquifers based on multioffset measurements, *Geophysics*, **74**(6), G47–G59,
860 https://doi.org/10.1190/1.3258342

861

862 Holbrook, W.S., Riebe, C.S., Elwaseif, M., Hayes, J.L., Basler-Reeder, K., Harry, D.L., Malazian, A.,
863 Dosseto, A., Hartsough, P.C. & Hopmans, J.W. 2014. Geophysical constraints on deep weathering
864 and water storage potential in the Southern Sierra Critical Zone Observatory, *Earth Surface Processes*
865 *and Landforms*, **39**(3), 366–380, http://dx.doi.org/10.1002/esp.3502

866

867 Jaunat, J., Huneau, F., Dupuy, A., Celle-Jeanton, H., Vergnaud-Ayraud, V., Aquilina, L., Labasque, T. &
868 Le Coustumer, P. 2012. Hydrochemical data and groundwater dating to infer differential flowpaths
869 through weathered profiles of a fractured aquifer, *Applied geochemistry*, **27**(10), 2053–2067,
870 https://doi.org/10.1016/j.apgeochem.2012.06.009

871

872 Kolbe, T., Marçais, J., Thomas, Z., Abbott, B.W., de Dreuzy, J.R., Rousseau-Gueutin, P., Aquilina, L.,
873 Labasque, T. & Pinay, G. 2016. Coupling 3D groundwater modeling with CFC-based age dating to
874 classify local groundwater circulation in an unconfined crystalline aquifer, *Journal of Hydrology*, **543**,
875 31–46, https://doi.org/10.1016/j.jhydrol.2016.05.020

876

877 Lapworth, D.J., MacDonald, A.M., Tijani, M.N., Darling, W.G., Gooddy, D.C., Bonsor, H.C. & Araguás-
878 Araguás, L.J. 2013. Residence times of shallow groundwater in West Africa: implications for
879 hydrogeology and resilience to future changes in climate, *Hydrogeology Journal*, **21**(3), 673–686,
880 https://doi.org/10.1007/s10040-012-0925-4

881

882 Legchenko, A. (eds.) 2013. *Magnetic resonance imaging for groundwater*. John Wiley & Sons.

883

884 Legchenko, A.V. & Shushakov, O.A. 1998. Inversion of surface NMR data, *Geophysics*, **63**(1), 75–84,
885 https://doi.org/10.1190/1.1444329

886

887 Legchenko, A., Comte, J.C., Ofterdinger, U., Vouillamoz, J.M., Lawson, F.M.A. & Walsh, J. 2017. Joint
888 use of singular value decomposition and Monte-Carlo simulation for estimating uncertainty in
889 surface NMR inversion, *Journal of Applied Geophysics*, **144**, 28–36,
890 https://doi.org/10.1016/j.jappgeo.2017.06.010

891

892 Legchenko, A., Descloitres, M., Vincent, C., Guyard, H., Garambois, S., Chalikakis, K. & Ezersky, M.
893 2011. Three-dimensional magnetic resonance imaging for groundwater, *New Journal of Physics*,
894 **13**(2), 025022, https://doi.org/10.1088/1367-2630/13/2/025022

895

896 Legg, I.C., Pyne, J.F., Nolan, C., McCardle, P., Flegg, A.M & O'Connor, P.J. 1985. *Mineral localities in*
897 *the Dalradian and associated igneous rocks of county Donegal, Republic of Ireland, and of Northern*
898 *Ireland*. Geological Survey of Ireland report series **RS 85/3**.
899
900 Long C.B., MacDermot C.V., Morris J.H. *et al*. 1992. *Geology of North Mayo*. GSI 1:100,000 bedrock
901 Series, Sheet 6 map and report, GSI, Dublin
902
903 Lubczynski, M. & Roy, J. 2004. Magnetic resonance sounding: New method for ground water
904 assessment, *Groundwater*, **42**(2), 291–309, http://dx.doi.org/10.1111/j.1745-6584.2004.tb02675.x
905
906 McConnell B.J. & Long C.B. 1997. *Geology of North Donegal: a geological description to accompany*
907 *the Bedrock Geology 1:100,000 Scale Map Series*. Sheet 1 and part of Sheet 2, North Donegal, GSI,
908 Dublin
909
910 Moe H., Craig M. & Daly D. 2010. *Poorly productive aquifers: monitoring installations and conceptual*
911 *understanding*. CDM and the Environmental Protection Agency, Dublin.
912
913 Nitsche, J. 2014. *Physical characterisation of groundwater flow systems of selected poorly productive*
914 *bedrock aquifers in Ireland*. PhD thesis, Queen's University Belfast, 248 p. + appendixes.
915
916 Neuman, S.P. 2005. Trends, prospects and challenges in quantifying flow and transport through
917 fractured rocks, *Hydrogeology Journal*, **13**(1), 124–147, https://doi.org/10.1007/s10040-004-0397-2
918
919 Pilatova, K. 2013. *Characterisation of Irish poorly productive aquifers using chemical and isotopic*
920 *tools*. PhD thesis, Queen's University Belfast, 332 p.
921
922 Rayner, S.F., Bentley, L.R. & Allen, D.M., 2007. Constraining aquifer architecture with electrical
923 resistivity imaging in a fractured hydrogeological setting, *Journal of Environmental & Engineering*
924 *Geophysics*, **12**(4), 323–335, https://doi.org/10.2113/JEEG12.4.323
925
926 Revil, A., Cathles, L.M., Losh, S. & Nunn, J.A. 1998. Electrical conductivity in shaly sands with
927 geophysical applications, *Journal of Geophysical Research: Solid Earth*, **103**(B10), 23925–23936,
928 http://dx.doi.org/10.1029/98JB02125
929
930 Ridge, M.J. 1983. A Combustion Method For Measuring The Cation Exchange Capacity Of Clay
931 Materials, *The Log Analyst*, **24**(03).
932
933 Robins, N.S. & Smedley, P.L. 1994. Hydrogeology and hydrogeochemistry of a small, hard-rock
934 island—the heavily stressed aquifer of Jersey, *Journal of Hydrology*, **163**(3-4), 249–269,
935 https://doi.org/10.1016/0022-1694(94)90143-0
936
937 Schulze-Makuch, D. 2005. Longitudinal dispersivity data and implications for scaling behaviour,
938 *Groundwater*, **43**(3), 443–456, http://dx.doi.org/10.1111/j.1745-6584.2005.0051.x
939
940 Sharp, J.M. (eds.) 2014. *Fractured Rock Hydrogeology*. CRC Press.
941
942 Singh, A. 2014. Groundwater resources management through the applications of simulation
943 modeling: a review, *Science of the Total Environment*, **499**, 414–423,
944 https://doi.org/10.1016/j.scitotenv.2014.05.048
945

946 Singhal, B.B.S. & Gupta, R.P. (eds) 2010. *Applied hydrogeology of fractured rocks*. Springer Science &
947 Business Media.

949 Skinner, D. & Heinson, G. 2004. A comparison of electrical and electromagnetic methods for the
950 detection of hydraulic pathways in a fractured rock aquifer, Clare Valley, South Australia,
951 *Hydrogeology Journal*, **12**(5), 576–590, https://doi.org/10.1007/s10040-004-0356-y

953 Smith R.A. 1991. *Newtownards: memoir for sheet N37 and part of N38*. Geological map 1:50000
954 scale, British Geological Survey, Keyworth, UK

956 Swineford, A. 1955. *Petrography of Upper Permian Rock in South-central Kansas*. University of
957 Kansas.

959 Thomas, E.C. 1976. The determination of Qv from membrane potential measurements on shaly
960 sands, *Journal of Petroleum Technology*, **28**(09), 1087–1096, https://doi.org/10.2118/5505-PA

962 UKTAG 2011. UK Technical Advisory Group on the Water Framework Directive, Defining & Reporting
963 on Groundwater Bodies, Working Paper Version V6.21/Mar/2011

965 Vouillamoz, J.M., Sokheng, S., Bruyere, O., Caron, D. & Arnout, L. 2012. Towards a better estimate of
966 storage properties of aquifer with magnetic resonance sounding, *Journal of hydrology*, **458**, 51–58,
967 https://doi.org/10.1016/j.jhydrol.2012.06.044

969 Vouillamoz, J.M., Lawson, F.M.A., Yalo, N. & Descloitres, M. 2014. The use of magnetic resonance
970 sounding for quantifying specific yield and transmissivity in hard rock aquifers: The example of
971 Benin, *Journal of Applied Geophysics*, **107**, 16–24, https://doi.org/10.1016/j.jappgeo.2014.05.012

973 Waxman, M.H. & Smits, L.J.M. 1968. Electrical conductivities in oil-bearing shaly sands, *Society of
974 Petroleum Engineers Journal*, **8**(02), 107–122, https://doi.org/10.2118/1863-A

976 Welch, L.A. & Allen, D.M. 2014. Hydraulic conductivity characteristics in mountains and implications
977 for conceptualizing bedrock groundwater flow, *Hydrogeology Journal*, **22**(5), 1003–1026,
978 https://doi.org/10.1007/s10040-014-1121-5

980 Wiklander, L. 1964. Cation and anion exchange phenomena, *Chemistry of the Soil*, **126**, 107–148

982 Worthington R. & Walsh J.J. 2011. Structure of Lower Carboniferous basins of NW Ireland, and its
983 implications for structural inheritance and Cenozoic faulting, *Journal of Structural Geology*, **33**,
984 1285–1299, https://doi.org/10.1016/j.jsg.2011.05.001

986 Zhou, Q., Liu, H.H., Molz, F.J., Zhang, Y. & Bodvarsson, G.S. 2007. Field-scale effective matrix
987 diffusion coefficient for fractured rock: Results from literature survey, *Journal of contaminant
988 hydrology*, **93**(1), 161–187, https://doi.org/10.1016/j.jconhyd.2007.02.002

Tables and captions

Table 1. *Summary and source of Waxman and Smits model parameters used to derive porosity values for the different aquifer units*

	Bulk resistivity[*] [ohm.m]	Water temperature[†] [°C]	Water electrical conductivity[†] [S/m]	Cementation factor[‡] [unitless]	Cation exchange capacity[§] [meq/100g]
Overburden	< 500	12.1 – 16.0	0.027 – 0.045	2.5	2.0 – 6.0[¶]
Broken zone	500 – 2500	12.1 – 16.0	0.027 – 0.045	2.5	2.0 – 6.0
Fissured zone	300 – 1000	12.8 – 14.2	0.029 – 0.050	2	5.2 – 18.7
Massive zone	1000 – 10 000	12.7 – 13.1	0.033 – 0.057	1.5	1.2 – 1.7

[*] 2D distribution obtained from ERT (see Results section).
[†] average values (summer 2009) recorded in boreholes (low temporal variability).
[‡] from Hartmann and Beaumont (1999).
[§] values calculated from mineralogical analysis and natural gamma log (see Results section).
[¶] same values as for the broken zone due to lack of in situ data.

Table 2. *Clay compositions in the different boreholes and resulting bedrock clay weight fraction and cation exchange capacity (CEC)*

	Muscovite[*] % vs tot. clay	Chlorite[*] % vs tot. clay	Illite[*] % vs tot. clay	Montm.[*] % vs tot. clay	Nat. γ[†] cps	Clay weight fraction[‡] %	Total CEC[‡] meq/100g
GO1							
Broken zone (transition)	58	27	7	8	116	51	6.0
Fissured zone (shallow)	40	20	22	18	111	51	**11.7**
Massive zone (deep)	66	34	0	0	102	43	1.7
GO2							
Broken zone (transition)	75	11	8	5	101	40	3.2
Fissured zone (shallow)	18	3	47	32	102	48	**18.7**
Massive zone (deep)	82	18	0	0	116	47	1.2
GO3							
Broken zone (transition)	77	14	5	4	78	30	2.0
Fissured zone (shallow)	28	5	40	27	41	16	**5.2**
Massive zone (deep)	82	18	0	0	116	47	1.2

[*] dominant clay minerals that affects natural gamma logging and rock bulk CEC. CEC (muscovite)~1 meq/g; CEC (illite)~10 meq/g; CEC (illite)~20 meq/g; CEC (montmorillonite)~90 meq/g (multiple sources, see Methods section).
[†] average natural gamma count per seconds from borehole logging.
[‡] Clay weight fraction and CEC calculated from individual clay CEC and natural gamma according to Revil *et al.* (1998).

1001 **Table 3**. *Summary of isotropic hydraulic conductivities obtained from pumping and recovery test*
1002 *interpretation and comparison with previous results*

Hydrogeological unit	Thickness from ERT [m]	Mean K [m/d]	K range [m/d]	Mean K from previous works[*] [m/d]	K range from previous works[*] [m/d]
Overburden	10 (in valley floor)	8.7	-	9	-
Broken bedrock (transition z.)	15-60	1.3×10^{-1}	$1\times10^{-1} - 2\times10^{-1}$	1	$7\times10^{-2} - 7$
Fissured bedrock (shallow z.)	5-40	1.0×10^{-2}	$3\times10^{-3} - 4\times10^{-2}$	$1\ 10^{-2}$	$1\times10^{-3} - 4\times10^{-2}$
Massive bedrock (deep z.)	>40	6.0×10^{-3}	$4\times10^{-3} - 8\times10^{-3}$	$1\ 10^{-2}$	$7\times10^{-3} - 6\times10^{-2}$

* initial hydraulic testing after drilling (Moe et al. 2010) using Horslev (infiltration tests) and Theis-Jacob (pumping tests)

1003
1004
1005 **Table 4**. *Recharge values recalculated using the water table fluctuation methods and the specific*
1006 *yield values derived from MRS. Borehole name suffixes SS (subsoil), T (transition) are derived from*
1007 *the codes listed in section Hydrogeological setting*

	Rainfall[*] [mm/y]	Water table cumulated rise[*] [m]	Specific yield[†] [%]	Calculated recharge [mm/y]	Calculated recharge [% of rainfall]
Hillslope					
GO1T 2010-2011	1134	13.6	0.75	102	9
GO1T 2011-2012	1433	19.7	0.75	147	11
GO2T 2010-2011	1134	8.8	1.57	138	13
GO2T 2011-2012	1433	16.8	1.57	264	19
Average				163	13
Valley floor					
GO3SS 2010-2011	1134	7.4	3	222	21
GO3SS 2011-2012	1433	11.7	3	351	24
Average				287	23

* from Cai & Ofterdinger (2016)
† from MRS, assuming specific yield = 0.5*MRS water content

1008
1009
1010 **Table 5**. *Details of key hydrogeological parameters and recharge values applied to Model 1 and 2*

	$Kmax$[*] [m/d]	$Kmin/Kmax$ [unitless]	Anisotropy angle [°]	Porosity[†] [%]	Recharge[‡] [mm/y]
Model 1					
Overburden	9	1	Isotropic	20	Valley floor: 95 (480)[§]
Broken zone	1 (0.2)[§]	1	Isotropic	4	Hillslope: 75 (370)[§]
Fissured zone	0.01 (0.002)[§]	1	Isotropic	0.2	NA
Massive zone	0.01 (0.002)[§]	1	Isotropic	0.01	NA
Model 2					
Overburden	8.6	1	Isotropic	7	Valley floor: 285
Broken zone	0.14	0.5	75 ° dip NW	3	Hillslope: 165
Fissured zone	0.014	0.3	85 ° dip SE	0.1-0.5	NA
Massive zone	0.008	0.1	65 ° dip SE	0.01	NA

* from Moe *et al*. (2010) for Model 1; from Comte *et al*. (2012) for Model 2
† from Comte *et al*. (2012) for Model 1; from Waxman and Smits' model and MRS results for Model 2 (Figure 7)
‡ from Cai & Ofterdinger (2016) for Models 1; recalculated values for Model 2 (Table 4)
§ values in brackets are final values after model calibration to observed heads in boreholes (K/5 and Recharge*5)

Figure captions

Fig. 1. *Study site physical setting maps; (**a**) site location within the Irish basement geological framework (modified from Geological Survey of Ireland 2006); (**b**) catchment boundary with location of hydrological monitoring infrastructures; (**c**) local interpretative geological map with location of the borehole clusters, the ERT profile and the MRS soundings.(**a**) and (**b**) modified from Comte* et al. *(2012).*

Fig. 2. *Generic hydrogeological conceptual model of weathered/fractured rocks aquifers in the context of the Irish terminology (modified from Comte* et al. *2012).*

Fig. 3. *Fracture pole density distributions (Schmidt net lower hemisphere projection) and orientations (fracture azimuth rose diagrams) from outcrops and boreholes (acoustic televiewer probe); blue points and arrows show the hydraulically active fractures unambiguously identified in boreholes (Nitsche 2014; modified from Comte* et al. *2012).*

Fig. 4. ERT results (**a**) and interpreted conceptual model of the weathered/fractured aquifer (**b**).

Fig. 5. *Comparison of hydraulic conductivities obtained from; (**a**) initial isotropic hydraulic test interpretations from Moe* et al. *(2010) used in Model 1; (**b**) refined isotropic interpretation from Comte* et al. *(2012); and (**c-e**) anisotropic K values used in Model 2, (**c**) K_{max}, (**d**) $K_{equivalent}$, and (**e**) K_{min}.*

Fig. 6. *Vertical distribution of MRS water content for the 8 MRS sounding (see locations on Figure 1) and comparison with the aquifer conceptual model units delineated from ERT (Figure 4).*

Fig. 7. *Spatial variations of storage properties derived from ERT and MRS geophysical data; (**a**) ERT resistivity model with location of approximate volume of investigation of the MRS soundings; (**b**) MRS water content logs; (**c**) ERT porosity calculated from Waxman & Smits' model. Hatched areas indicate the unsaturated zone for which saturated Archie and Waxman & Smits models used are not applicable.*

Fig. 8. *Conceptual aquifer geometries implemented in the numerical models: (**a**) generic tabular structure of weathered/fractured layers from borehole interpretation (Model 1); (**b**) complex layered structure derived from geophysical data reconciled with borehole logs (Model 2). 1: Overburden (alluvial and glacial sediments); 2: Broken bedrock (transition zone); 3: Fissured (shallow) bedrock; 4: Massive (deep) bedrock; 5: Substratum (very low productivity).*

Fig. 9. *Simulation results for Model 1 (**a,b,c**) and Model 2 (**d,e,f**) showing groundwater seepage rates at the model surface, Darcy's fluxes variations across the transect (**a,d**), groundwater mean flowpaths (**b,e**), and groundwater ages (**c,f**).*
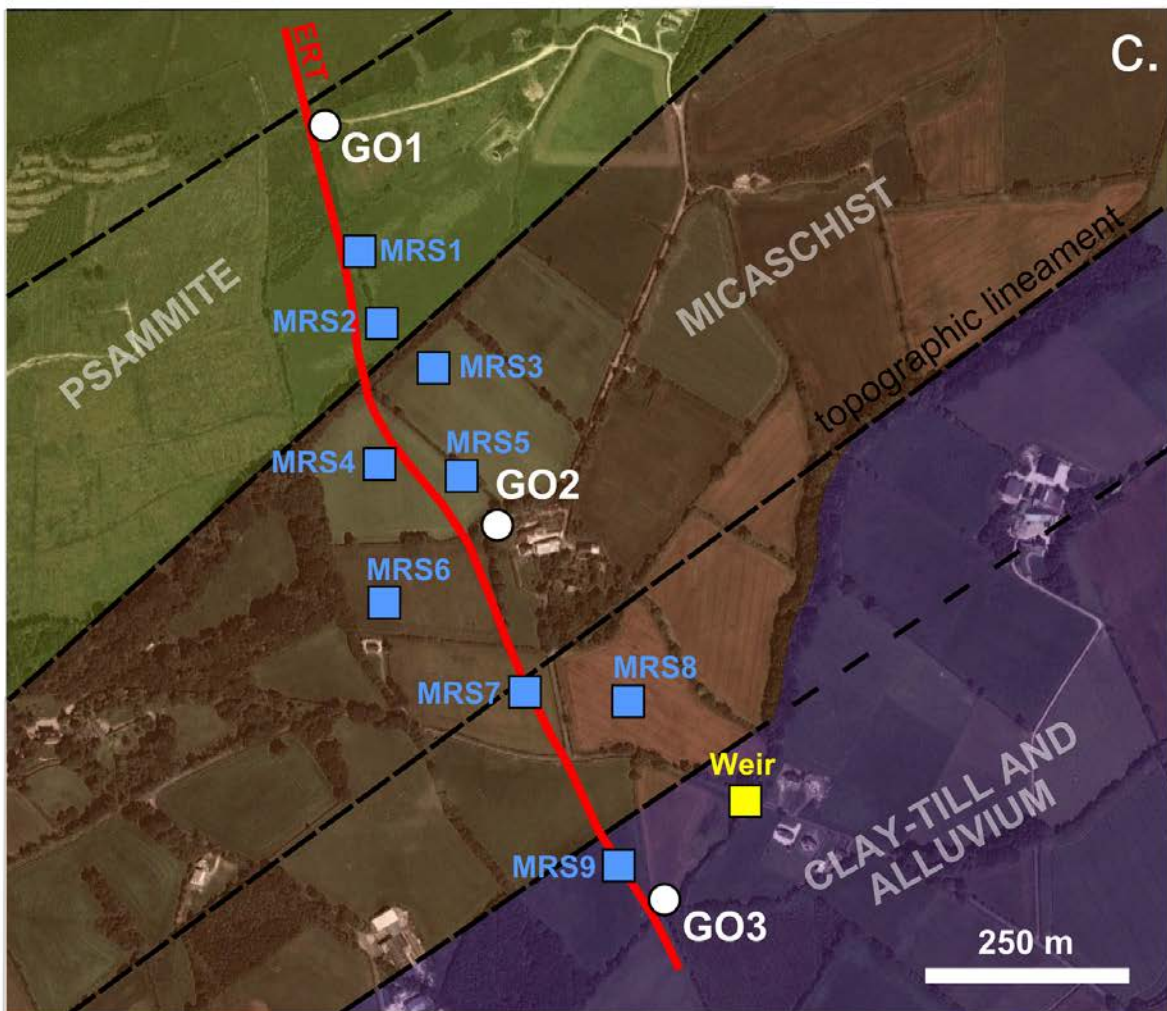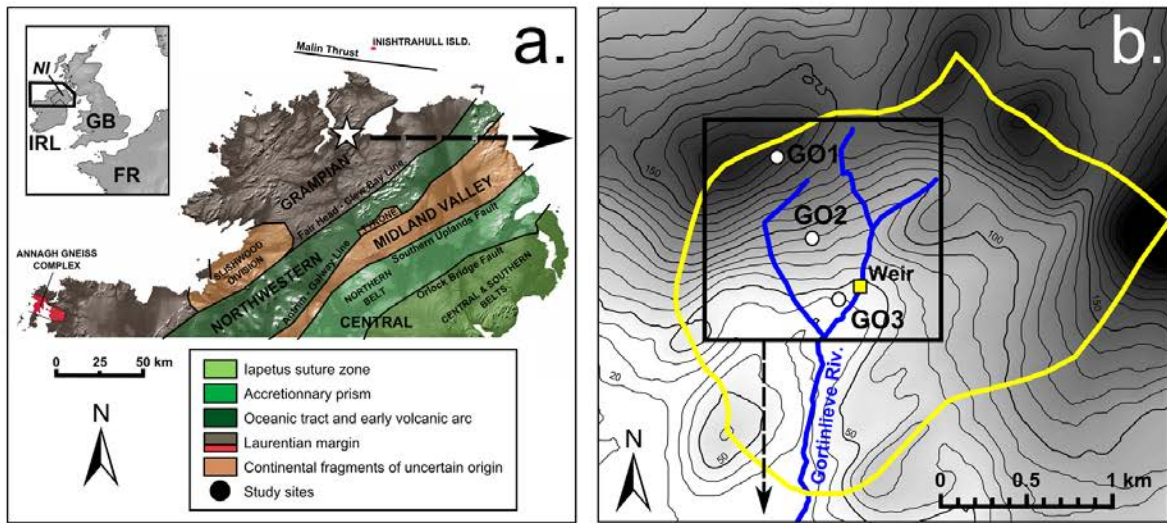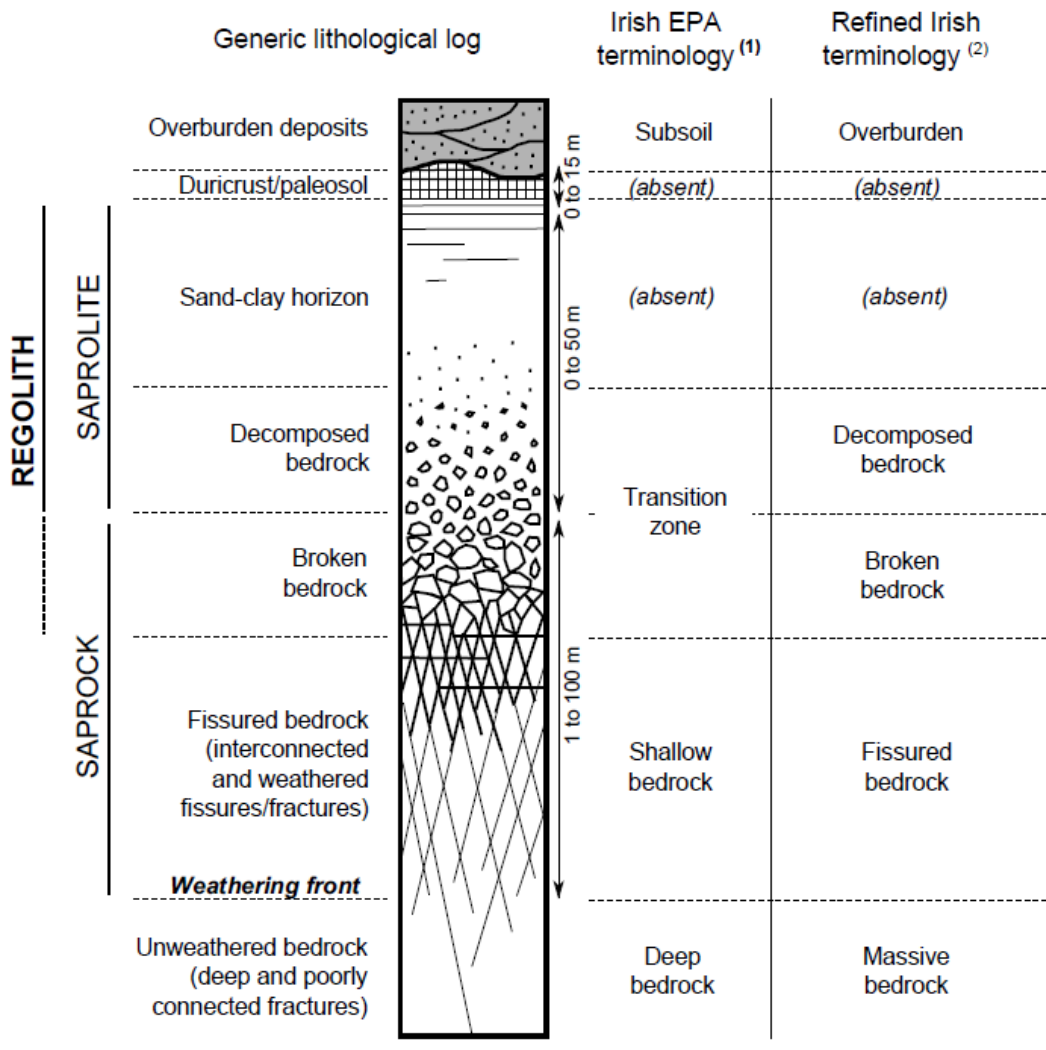
Fig. 10. *Relative distributions of groundwater flow rate (as % of total flow) in the four conceptual aquifer units (overburden, broken, fissured and massive bedrock) for the two models considered. The massive bedrock here also includes the deeper levels shown in Figure 8.*

Fig. 11. *Modelled groundwater ages in the different boreholes for the two model cases. The hatched area indicates groundwater ages that are older than the modern period of high atmospheric Tritium levels, and inconsistent with measured Tritium concentrations in boreholes samples.*
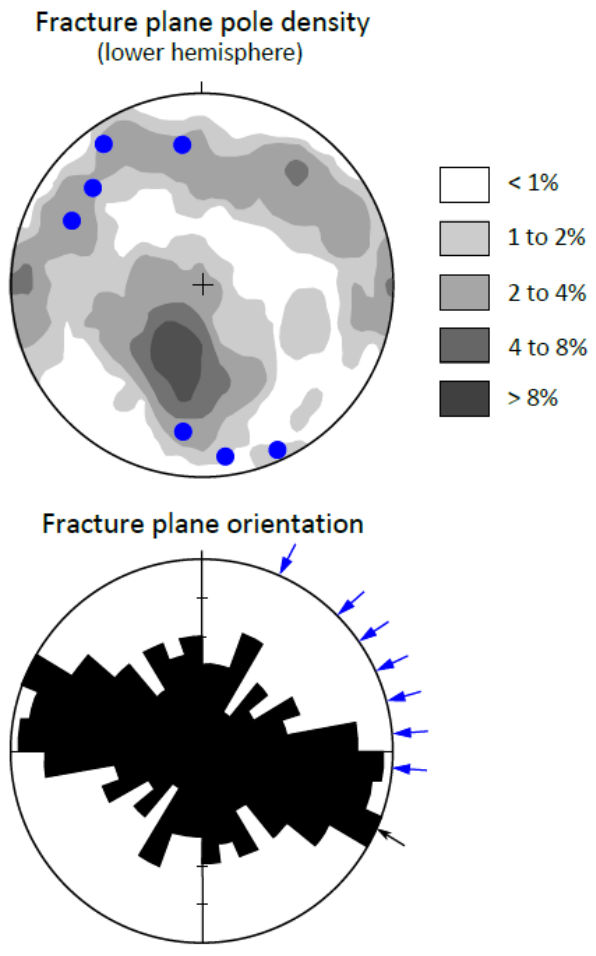
1060   Figure 1

1061
1062

1063   Figure 2

Figure showing Generic lithological log, Irish EPA terminology (1), and Refined Irish terminology (2).

Generic lithological log:
- REGOLITH
  - SAPROLITE
    - Overburden deposits
    - Duricrust/paleosol
    - Sand-clay horizon
    - Decomposed bedrock
  - SAPROCK
    - Broken bedrock
    - Fissured bedrock (interconnected and weathered fissures/fractures)
    - *Weathering front*
    - Unweathered bedrock (deep and poorly connected fractures)

Depth scale: 0 to 15 m; 0 to 50 m; 1 to 100 m

Irish EPA terminology (1):
- Subsoil
- (absent)
- (absent)
- Transition zone
- Shallow bedrock
- Deep bedrock

Refined Irish terminology (2):
- Overburden
- (absent)
- (absent)
- Decomposed bedrock
- Broken bedrock
- Fissured bedrock
- Massive bedrock

(1) After Moe *et al.* (2010)
(2) After Comte *et al.* (2012)

1064
1065

1066   Figure 3

Fracture plane pole density
(lower hemisphere)

☐	< 1%
☐	1 to 2%
☐	2 to 4%
☐	4 to 8%
■	> 8%

Fracture plane orientation

n = 237

1067
1068

1069   Figure 4
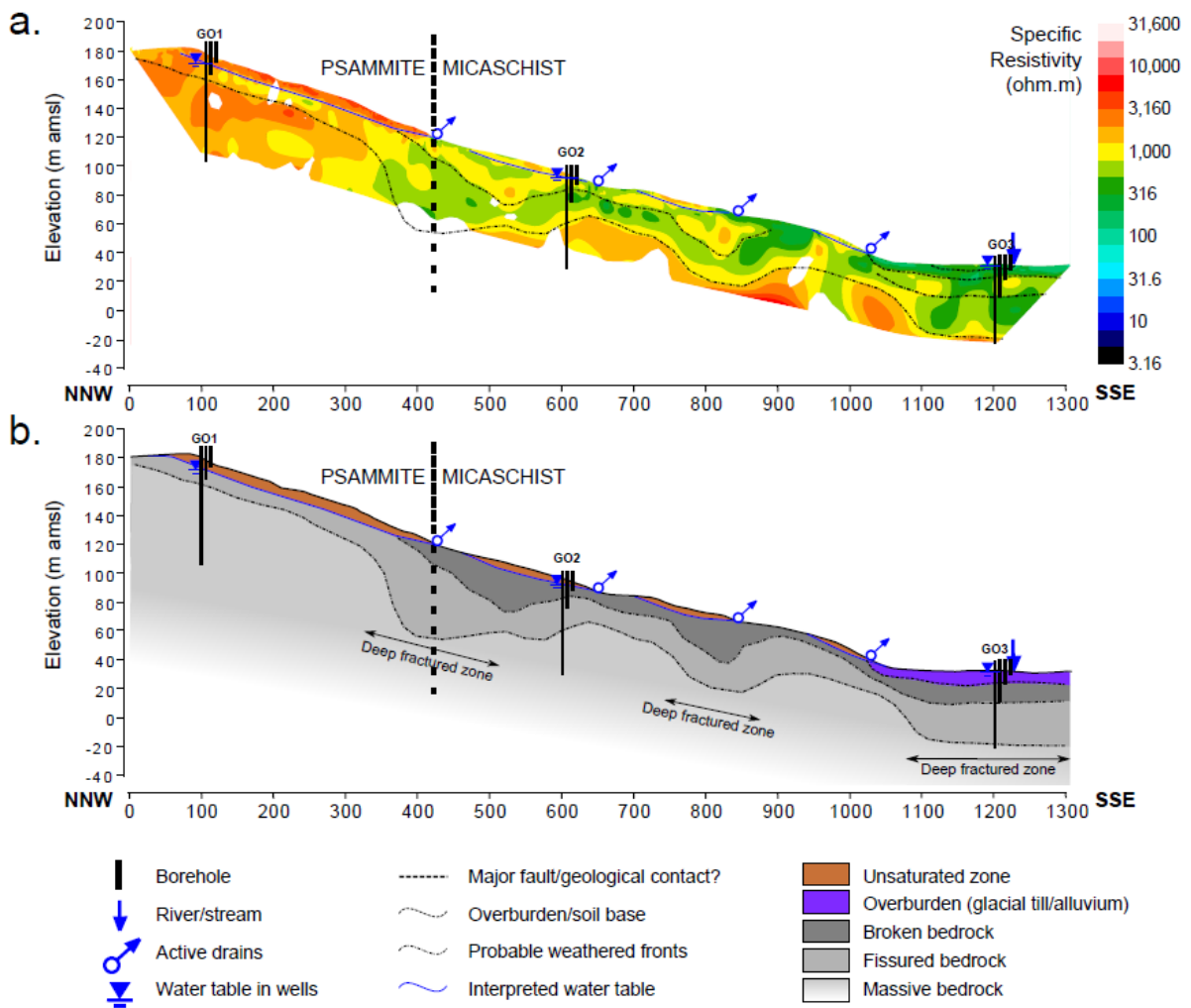
1072   Figure 5
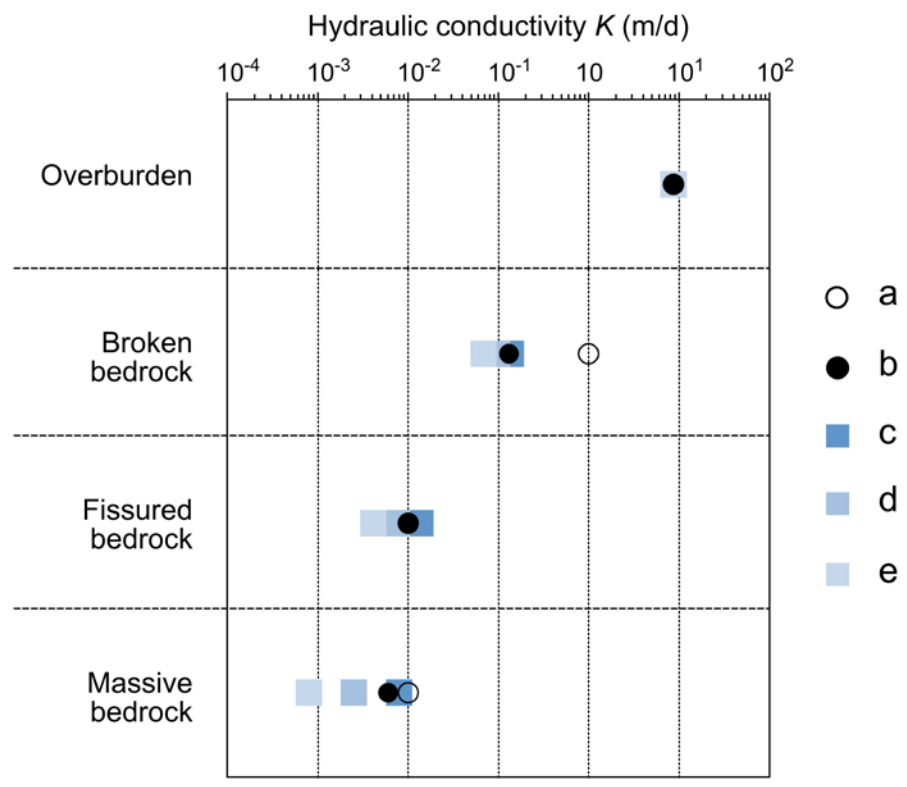
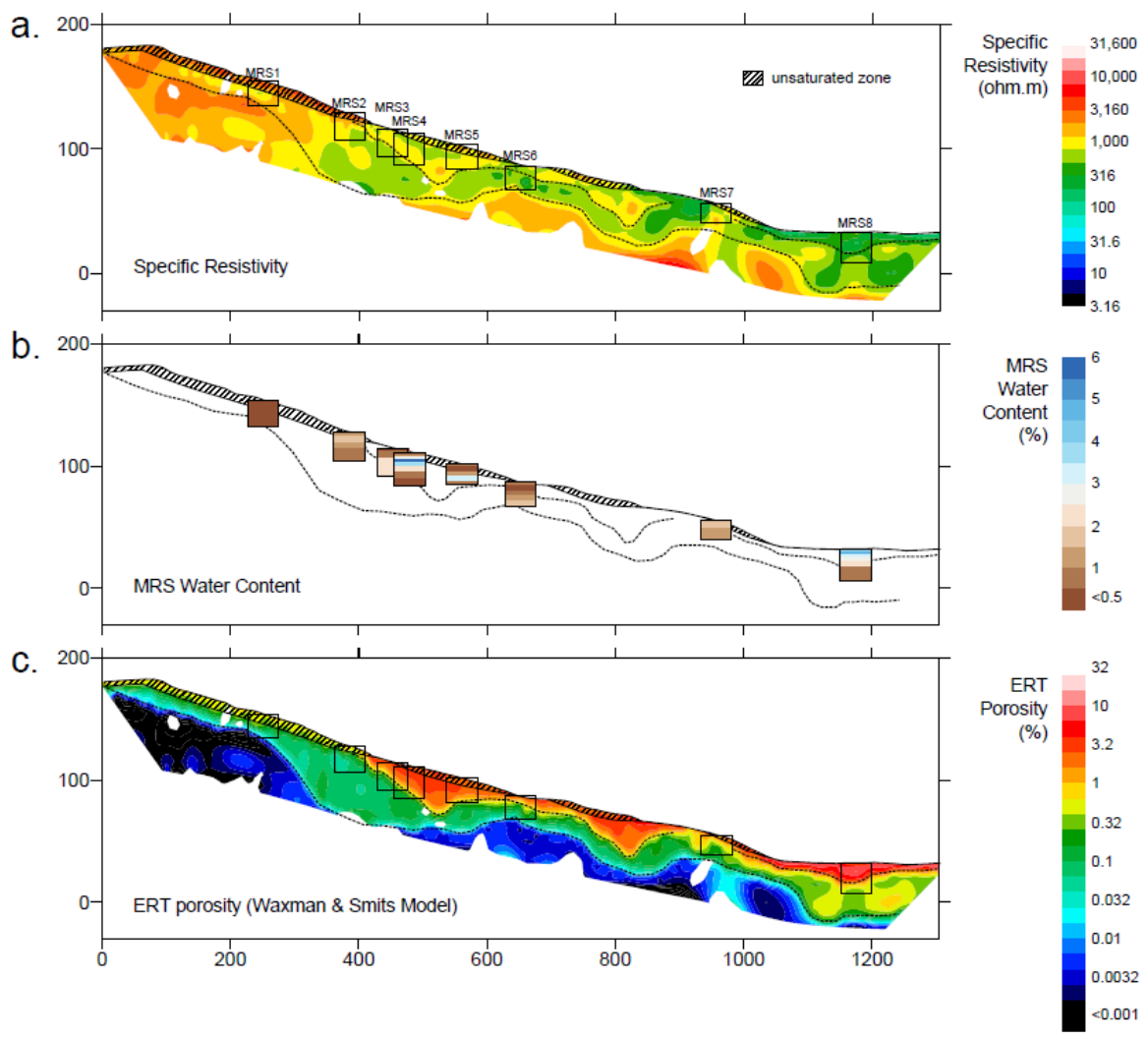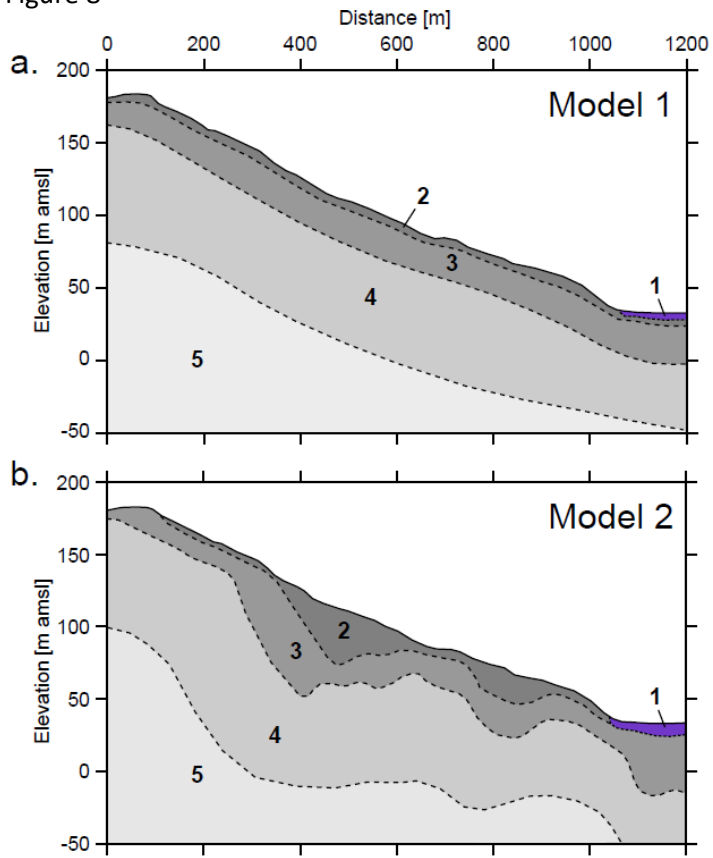1073
1074
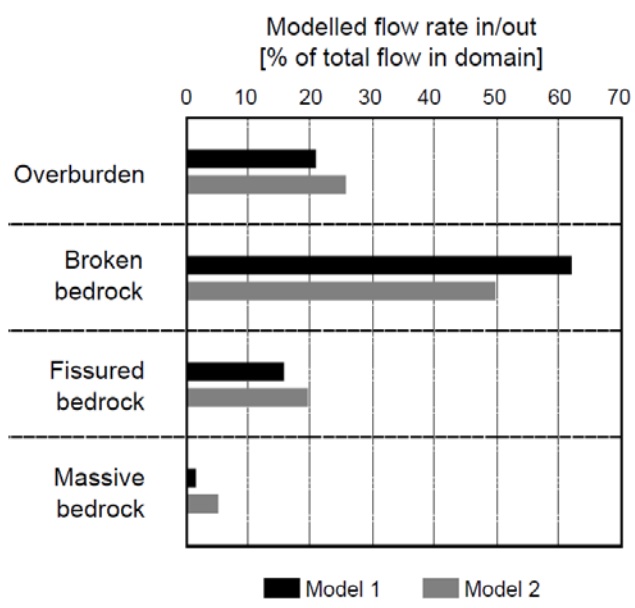
1075   Figure 6
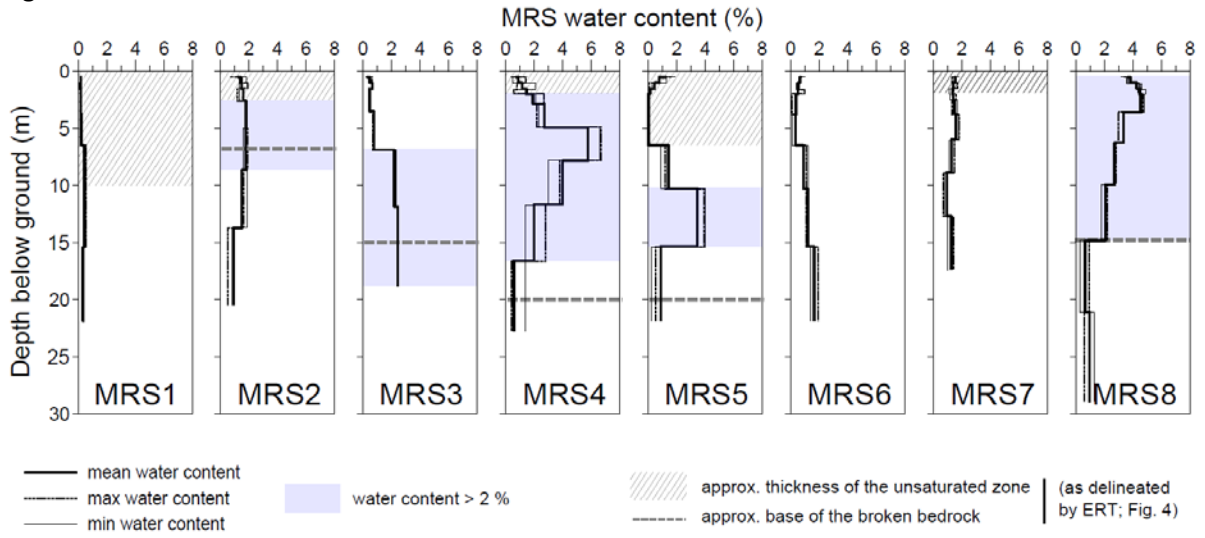
1078   Figure 7

1079
1080

1081   Figure 8

1082
1083

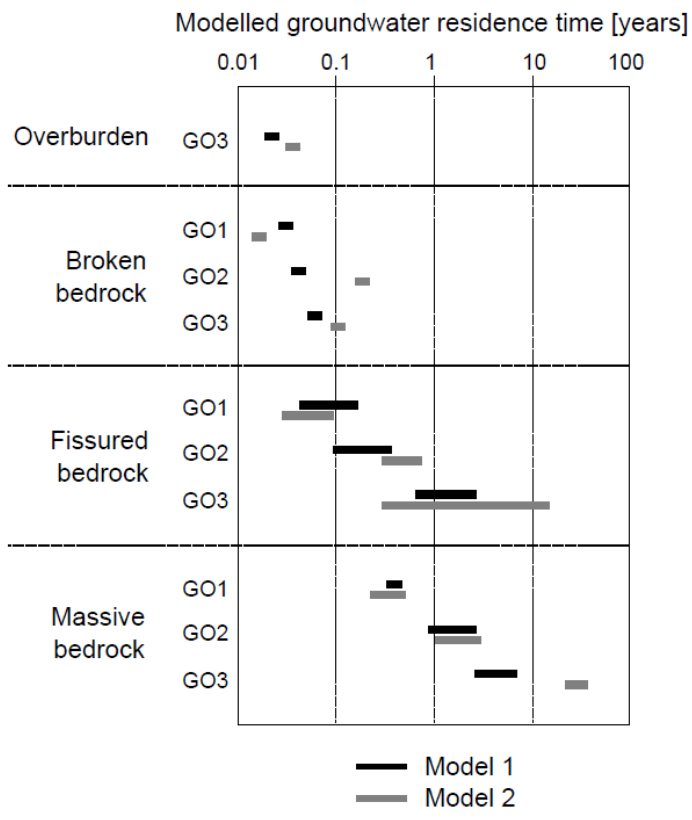1084   Figure 9

1085
1086

1087   Figure 10

Modelled flow rate in/out
[% of total flow in domain]

Model 1   Model 2

1088
1089

1090   Figure 11

Figure 11

1091